RESEARCH ARTICLE

Basin Research

IAS EAGE

WILEY

Identification and differentiation of vertical movement through morphological changes and stratigraphic imprint: Two distinct uplifting mechanisms in the upper Calabrian accretionary wedge, western Ionian Sea

Bruna T. Pandolpho | Morelia Urlaub | Christian Berndt | Jörg Bialas

GEOMAR Helmholtz Centre for Ocean Research Kiel, Kiel, Germany

Correspondence
Bruna T. Pandolpho, GEOMAR Helmholtz Centre for Ocean Research Kiel, Kiel, Germany.
Email: bpandolpho@geomar.de

Abstract

The seafloor morphology reflects both past and on-going sedimentary, oceano-graphic and tectonic processes. Vertical movement is one of the drivers respon-sible for reshaping the seafloor through forming steep flanks that decrease slope stability, favour landslides, change current paths, form minibasins and control the sediment deposition, distribution and geometry. Here, we make use of these interactions to derive vertical movements and constrain the active tectonic pro-cesses at the western termination of the upper Calabrian accretionary wedge from the integrated analysis of bathymetric, backscatter, surface attributes and high-resolution reflection seismic data. Within this area, we identify two types of deformational features and mechanisms that affect the depositional, erosional and tectonic processes at different scales. These include the deviation of chan-nels, landslide scars, mass transport deposits (MTDs), separated drifts, sediment waves, lineaments and offset seafloor structures. The first type (long-wavelength uplift) is an uplifted 22-km-wide region, in which seismic onlap relationships and the dip of deep reflectors suggest long-lasting but slow tectonic uplift affect-ing sedimentation, and the second type (short-wavelength uplift) includes three narrow elongated structures and one circular dome encircling the first region of uplift. We interpret that the first type of uplift feature was caused by tectonic de-formation, while the second type is interpreted as formed by the fast uplift, tilting and faulting of modern sediments caused by diapirism due to rapid sedimenta-tion in response to the first tectonically driven uplift. The study provides insight into the complex interaction of tectonic and sedimentary processes in the upper Calabrian accretionary wedge.

KEYWORDS
geomorphology, Ionian Basin, proxy, uplift

1 | INTRODUCTION

The seafloor, its landforms and its landscapes are the result and combined effect of tectonic, sedimentary, oceanographic and biological processes (Micallef, Krastel, & Savini, 2018; Micallef et al., 2022; Posamentier et al., 2022). Hence, seafloor morphology holds information on many different processes that act over a wide range of temporal and spatial scales. Leveraging this archive, however, requires identifying and untangling the individual processes and their interactions.

Recent progress in seafloor geodesy provides new insights into geological processes that cause short-term seafloor deformation, however, this field still relies mostly on geologic interpretations. Large-scale seafloor topographic highs in otherwise relatively flat areas, like the continental rise and abyssal plains, can have numerous possible origins such as gravitational mass transport deposits or active uplifting through subsurface processes. In both cases, the seafloor structure interacts with the sedimentary system and/or the oceanographic setting, changing its original seafloor morphology and forming new features that record this interaction. For vertical movement, the resulting interaction can be even more complex, with different morphologies formed by inactive and active uplift. A thorough understanding of the seafloor morphology of and around a topographic high may thus allow deducing the origin, sequence and timing of its vertical movement.

The Ionian Sea in the eastern Mediterranean (Figure 1) is a complex geodynamic area that records a long history of sedimentation, erosion and magmatic and tectonic activity (Gutscher et al., 2017). Off the eastern coast of Sicily, the north-western Ionian Basin hosts evidence of gravity-driven and along-slope sedimentary processes, canyon and channel systems, volcano activity, strike-slip faults and possible diapirism (e.g. Gutscher et al., 2017). Unravelling these geological processes is crucial as they influence a range of natural hazards. These include major earthquakes such as the 1908 Messina earthquake—for which there is still no satisfactory explanation—and the stability of the seaward flank of Mount Etna that has failed in major tsunamigenic sector collapses (Ryan & Heezen, 1965). Hence, improving the understanding of the active geological processes in this area will contribute to regional hazard assessments.

Within the upper Calabrian accretionary wedge, a distinct topographic high of nearly $260\,km^2$ dominates a stretch of the basin between 1900 and 2100 m water depth (Figure 1). Argnani and Bonazzi (2005) first interpreted the area as a compressional feature and Polonia et al. (2017) later proposed that this structure has been formed by serpentinite diapirs. The aim of this work is to assess the sedimentary and tectonic processes that shape this region with a particular focus on the identification of seafloor uplift and its effects on subsequent sedimentation.

Highlights

- Indirect evidence for vertical movement/uplift evolution imprinted on the seafloor.
- Seafloor uplift inferred from changes in the sedimentary and oceanographic processes.
- Two uplifting mechanisms with different geological drivers and time scales that are intrinsically linked.
- Indications for salt diapirs within the upper Calabrian accretionary wedge.
- Development of a morphological archive that can be used to decipher vertical motion in complex geological areas.

The first objective is to determine which areas have been uplifted (i.e. changes in the seafloor morphology and elevation of the seabed) and what controlled the timing and reason for uplift. The second objective is to determine the implications of uplift for subsequent channelling of sediments and their deposition.

2 | REGIONAL SETTING

2.1 | Tectonic setting

The Ionian Sea is shaped by the convergence of the Eurasian–African plates. Within the Ionian Sea, the Calabrian accretionary wedge is the most important structure. It has a narrow retreating slab formed by the NW dipping Calabrian–Tyrrhenian subduction zone (Faccenna et al., 2014). It is bordered to the SW by a subduction tear-edge propagator (STEP) fault and to the east by the thrust fault and compression system from the collision with the Western Mediterranean Ridge. The exact placement of the STEP fault is still debated, being placed along with the Ionian fault (Barreca et al., 2019; Polonia et al., 2016, 2011), the Alfeo fault system (Gallais et al., 2013; Gutscher et al., 2019; Gutscher et al., 2015; Gutscher et al., 2017; Maesano et al., 2020) or the Malta–Hyblean Escarpment (Argnani & Bonazzi, 2005; Argnani et al., 2013; Gambino et al., 2021) (locations at Figure 1a).

The Malta Escarpment is a delimitation between the African continental and oceanic plates, marking the transition between the Pelagian platform and the Ionian Basin. At the upper Calabrian accretionary wedge, the Malta Escarpment is characterized by three main NNW–SSE east-dipping, slightly oblique normal extensional faults that are extremely relevant for the seismotectonic framework, with high seismic potential (M > 7), and the sedimentary processes of the western Ionian Basin (Argnani & Bonazzi, 2005; Gambino
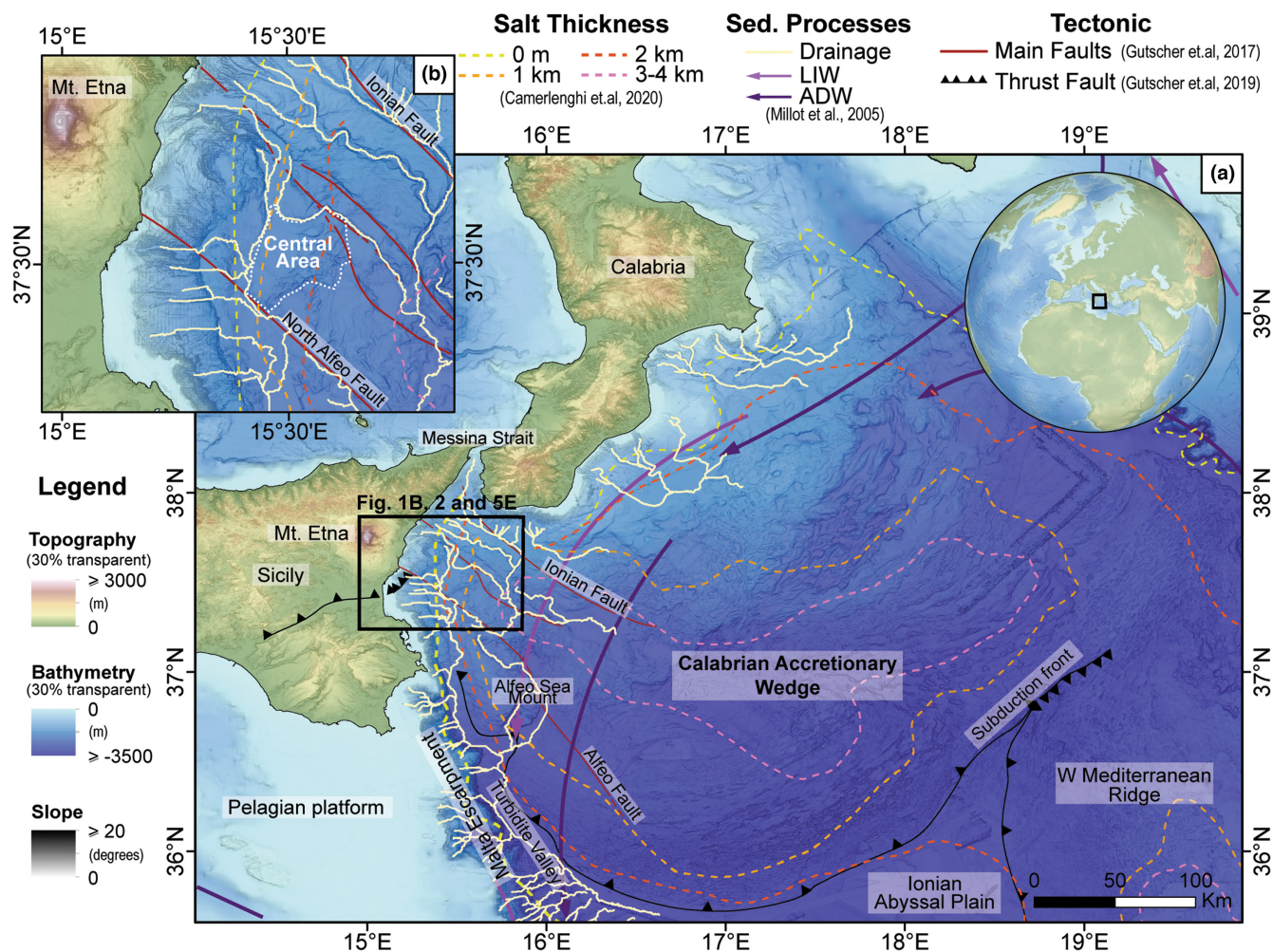
FIGURE 1 (a) Tectonic and sedimentary processes in the Ionian Basin, along with the salt thickness proposed by Camerlenghi et al. (2020). (b) Zoom in the main study area, named Central Area, within the upper Calabrian accretionary wedge.

et al., 2021). Sedimentary basins originated from the differential subsidence along the normal/extensional faults in the northern sector of the Malta Escarpment (as the Turbidite Valley of Gutscher et al., 2015). East of the Malta Escarpment, these basins are affected by a contractional deformation or folding leading to seafloor uplifting (as the uplifted areas by Argnani & Bonazzi, 2005), most probably related to transpression or strike-slip motion since Late Miocene–Pliocene, being simultaneous to the extension since the Pliocene (Gambino et al., 2021). From the mapped uplifted areas of Argnani and Bonazzi (2005), the one north of Syracuse is the main focus of this study and the main study area, referred to here as Central Area (Figure 1b).

Post-Messinian strike-slip deformation is the prevailing kinematics within the Calabrian accretionary wedge overlaying upper plate (Gambino et al., 2021; Gutscher et al., 2019). A series of long NW–SE-oriented dextral strike-slip faults are evident on the seafloor east of Mt. Etna and south of the Messina Strait (Gutscher et al., 2019; Gutscher et al., 2015; Gutscher et al., 2017). Signs of

mixed fault kinematics, that is, thrust and normal faulting, are explained by alternating transtensional and transpressional deformation (Gutscher et al., 2015; Gutscher et al., 2017). Among the major strike-slip faults, the right-lateral, 140-km-long, NW–SE-trending, Alfeo fault system is the most active (Gutscher et al., 2019). Commonly divided into north and south settings, the North Alfeo fault portion reaches into our study area, bounding the Central Area from the SW (Figure 1b).

The study area in the NW Ionian Basin is flanked by Europe's largest active volcano. Mount Etna was built up over the past 500 ka on the eastern coast of Sicily during the Neogene convergence (Branca et al., 2011). The volcano's south-eastern flank, which reaches well into the NW Ionian Sea, is unstable and slides into the Ionian Sea at rates of 3–5 cm per year (Solaro et al., 2010). A basement high in 1800 m water depths west of the study area separates the deformed and undeformed strata and thus appears to mark the limit of the rapidly eastwards moving part (Urlaub et al., 2022).

2.2 | Sedimentary processes and oceanographic setting

Within the upper Ionian Basin, the sedimentary processes are dominated by gravitational sediment transport. Several canyons cut the Catania shelf and can be mapped through the Ionian Basin (e.g. Gutscher et al., 2017). The canyon–channel systems of the steep continental slope east of Sicily provide the sediments that fill the small basins at the foot of the slope (Urlaub et al., 2022) and spill into the Turbidite Valley along the Malta Escarpment (Gutscher et al., 2015). Telecommunication cable breaks (Polonia et al., 2017; Ryan & Heezen, 1965), landslide scars and landslide deposits (Billi et al., 2008; Gross et al., 2016; Schambach et al., 2020) are all evidence for frequent gravitational sediment transport from the continental slope into the basin.

Other sedimentary processes and deposits include contouritic features along the Malta Escarpment (Rebesco et al., 2021). North and south of the study area, contourites associated with moats, drifts and large sediment waves have been described previously (e.g. Barreca et al., 2019; Micallef et al., 2018; Pepe et al., 2018; Rebesco et al., 2021). These features have been associated in this area with the flow of bottom currents, mainly the Levantine Intermediate Water (LIW) and the Adriatic Deep Water (ADW) (e.g. Marani et al., 1993; Pepe et al., 2018; Rebesco et al., 2021). The LIW and the ADW are the two main water masses in the Mediterranean Sea (Millot & Taupier-Letage, 2005). The LIW has the largest volume of any water mass formed in the Mediterranean Basin. Even though this water mass is easily recognized in the western Mediterranean Sea, its detailed description of the eastern Mediterranean Sea and Ionian Basin is still lacking. Within the Ionian Basin, both the LIW and ADW flow southward (from north to south, Figure 1a), the first with a very saline and relatively warm water mass that spreads at intermediate depths, while the second fills the deepest parts of the Ionian and Levantine Basins (Skliris, 2014).

Recently, Rebesco et al. (2021) mapped contourite deposits along the Malta Escarpment. The sediment waves are 50 m in height and have a 2.5-km-long wavelength. Rebesco et al. (2021) conclude that the waves migrated up-current (northward) since about 500 ka, suggesting a predominant along-slope southward flowing bottom current. The sediment waves' origin is linked to the increase in the sediment input to the Ionian Basin over time that results from neotectonic uplift in NE Sicily and Calabria, and the steady and low-energy bottom current that picked up at the Mid-Pleistocene (Rebesco et al., 2021).

2.3 | Messinian evaporites

The Messinian (from 7.246 to 5.333 Ma) is an important stratigraphic unit in the Mediterranean Sea. The Messinian salinity crisis (MSC), which started around 5.96–5.97 Ma, led to the deposition of a thick sequence of evaporites (Roveri et al., 2014). During this period, a sudden sea-level drop due to the closure of the Gibraltar Strait and intermittent connection of the Mediterranean Sea and the Atlantic Ocean resulted in shallow salty basins. This led to the massive deposition of evaporites in the basin and major erosional unconformities within the MSC shallow (margin erosion surface, MES) and deep waters (bottom, internal and top erosional surfaces) (Camerlenghi et al., 2020; Roveri et al., 2014). Offshore, the MES splits into the bottom erosional surface (BES) or bottom surface (BS), and the top erosional surface (TES) or top surface (TS) of the MSC depending on the evidence of erosion (Roveri et al., 2014). In general, the unconformities or erosional surfaces are interpreted as a subaerial result of the sea-level drop linked to the MSC, either before (in the case of the MES) or at the last stage of the MSC (in the case of the TES) (Roveri et al., 2014).

Even though drilling confirms the presence of salt in the Ionian Basin (Hsu et al., 1978), the spatial extent of the salt deposits below the Pliocene-to-Quaternary sedimentary fill is still a subject of discussion, especially in the northern Ionian Basin. The scarce deep reflection seismic lines, and difficulties in mapping salt by high-resolution seismic data, make it difficult to interpret the salt extent north of the Ionian abyssal plain (Camerlenghi et al., 2020). For that reason, many authors describe the Ionian Sea as having an external evaporitic wedge along the Calabrian ridge and an internal clastic wedge within the upper Calabrian accretionary wedge, where our main study area is located (e.g. Gutscher et al., 2017; Polonia et al., 2016). Only recently Camerlenghi et al. (2020) have proposed a new evaporite distribution that comprises the entire Ionian Basin (Figure 1a) based on the interpretation and interpolation of multiple-vintage multichannel seismic reflection data. The authors suggest up to 2 km of Messinian evaporites for our main study area (Figure 1b). However, refraction seismic lines crossing the southern part of the study area with a vertical resolution of ca. 1 km do not resolve a salt layer (Dellong et al., 2018).

3 | DATA AND METHODS

3.1 | Bathymetric data

Bathymetric datasets from two different surveys were merged in order to cover the main study area. Survey

SO277 (2020) onboard RV SONNE, used a hull-mounted Kongsberg multibeam echosounder system EM122 for depths between 1000 and 2300 m, while EM710 was recorded in areas with depths shallower than 1000 m (Urlaub et al., 2022). During the RV Meteor, survey M86/2, the hull-mounted Kongsberg EM122 was used (Krastel et al., 2012). The final merged bathymetry has a 30-m-grid spacing. Gaps in the grids were filled with a grid of coarser spacing from Gutscher et al. (2017).

Multibeam backscatter data for both surveys (Urlaub et al., 2022) were also used in our analysis. Backscatter data describe the amount of energy that is reflected back to the transducer, which in turn is related to the in sonification, the angle of the seabed and its acoustic properties. In general, high-intensity values are associated with coarse-grained sediments and/or rough seabed (high rugosity and reflection/backscattering), while low values are associated with fine-grained sediments or gentle slopes (low rugosity and backscattering) (e.g. Brown et al., 2019; Lurton & Lamarche, 2015).

3.2 | Surface attributes

Surface/terrain attributes were calculated from the bathymetric data to enhance features not directly visible in the topographic maps. Using the geographic information systems (GIS) ArcGIS and QGIS combined with the geoprocessing tools of Benthic Terrain Modeller (BTM) (Walbridge et al., 2018) and the Relief Visualization Toolbox (RVT) (Kokalj & Hesse, 2017), a series of quantitative analyses in the bathymetric datasets were made. The Benthic Terrain Modeller uses a combination of spatial analysis algorithms resulting in intermediate grid products. The Bathymetric Position Index (BPI), one of the BTM products, quantifies the difference between the Z value of a cell (depth) compared to the surrounding cells within a defined neighbourhood (i.e. an annulus, excluding immediately adjacent cells for the mean surrounding elevation). The result can be used to classify landscape features such as valleys, plains and hilltops based on the changes in slope position (Walbridge et al., 2018). Positive values represent elevational highs (e.g. crests and ridges) and negative values represent structural lows (e.g. depressions and valley bottoms).

The Bathymetric Position Index parameters of the annulus use a scale factor that is dependent on the geomorphic features to be enhanced and the bathymetry grid available. The outer radius is dependent on the scale of the geometric features to be investigated and should be equal to the feature size divided by the bathymetry cell size, while the inner radius is defined as 1/10 of the outer radius (Dillon, 2016; Weiss, 2001). In our analysis, the annulus was defined as 30 for the outer radius and 3 for the inner radius taking into consideration the topographic ridges width of approximately 870 m and a bathymetric grid resolution of 30 m.

The Sky View Factor (SVF), part of the Relief Visualization Toolbox, can be used to show relief characteristics. It is an alternative method of relief mapping overcoming hill-shading direct/preferential illumination. SVF is based on a uniform diffuse illumination that represents the portion of the sky visible from a celestial hemisphere (Zakšek et al., 2011). Unlike shading techniques, SVF does not contain any horizontal displacement. SVF values range from 0 to 1. Lower values closer to 0 (dark colours) are regions not completely visible 'from the sky' or the celestial hemisphere; they represent sinks, depressions and lower parts of slopes or cliffs, for example. Higher values closer to 1 (bright colours) represent regions almost entirely seen 'from the sky' (celestial hemisphere), which is the case of exposed features like planes, ridges and peaks (Zakšek et al., 2011). This technique enhances the visibility of small-scale features independent of their shape and orientation. A general filter radius of 10 m (Kokalj & Hesse, 2017) was used.

3.3 | Seismic data

The high-resolution 2D multichannel seismic datasets from POS496 and M86/2 combined comprise a total of 25 profiles (Figure 2). During RV POSEIDON cruise POS496 in 2016, a Sercel 0.4 L mini GI-gun was used along with
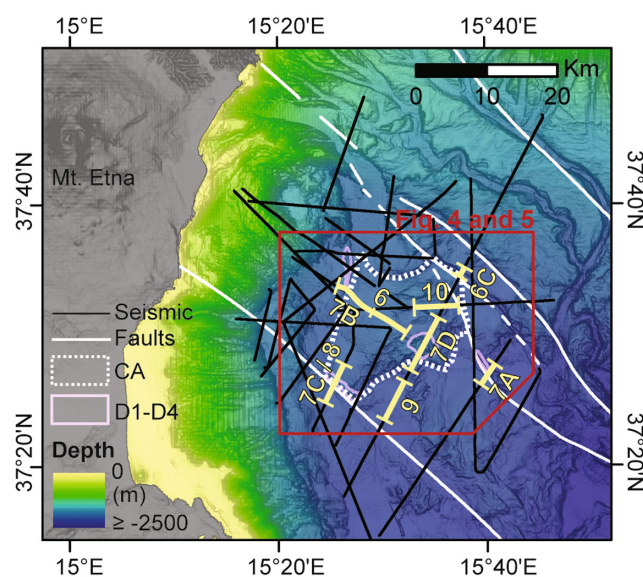

FIGURE 2 Overview of the main study area and its surroundings, location in Figure 1. Indication of the seismic lines crossing the main study area, the Central Area (white dash line) and features D1–D4 (pink line). Bold yellow lines and numbers designate further figures' annotation.

a GEOMETRICS GeoEel digital solid-state streamer with 80 channels and 1.5625 m group spacing (Krastel, 2016). Processing included bandpass filtering, geometry setup, normal-move-out correction, common mid-point stacking and a finite-difference time migration (with a constant velocity of 1500 m/s) (Gambino et al., 2021; Gross et al., 2016). Survey M86/2 was acquired with RV METEOR between December 2011 and January 2012. Data were acquired with a 1.7 L GI-gun and a 104-channel GEOMETRICS GeoEel digital streamer with a group interval of 1.5625 m. Processing included bandpass filter, de-spiking, common mid-point stacking, normal-move-out correction (with a constant velocity of 1500 m/s) and finite-difference time migration (with a constant velocity of 1500 m/s) (Gross et al., 2016; Urlaub et al., 2022). Given the dominant frequency of 130 Hz, the near-surface resolution of the data is about 2 m horizontally and 5 m vertically.

4 | RESULTS

The morphology (surface) and the stratigraphy (subsurface) are described separately and grouped into topographic, erosional, depositional and tectonic features
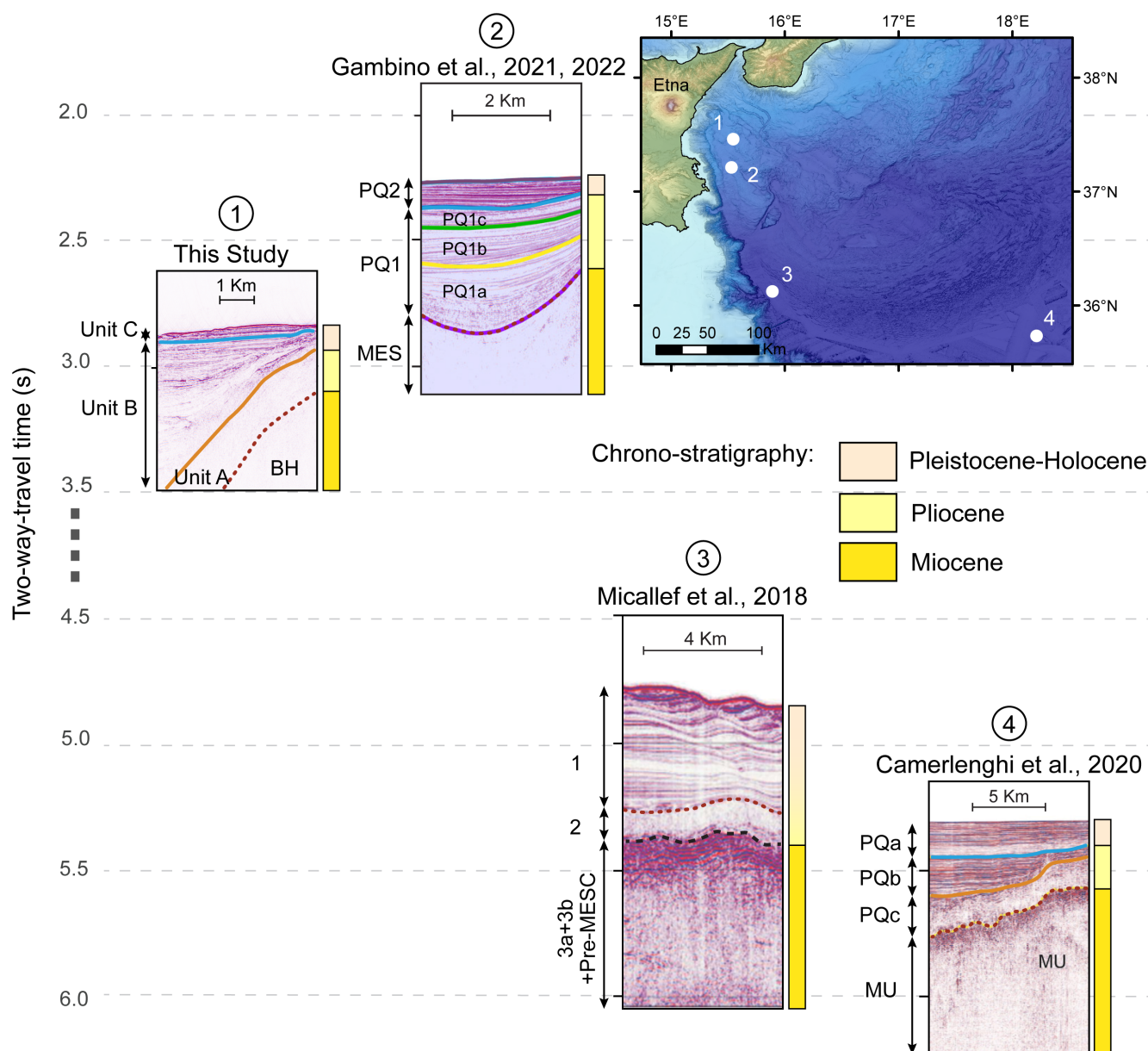

FIGURE 3 Comparison in two-way travel time (TWT) in seconds scale of the seismic facies and stratigraphy on the Ionian Basin. The figures are presented according to their location within the basin. The main boundaries (in blue, orange and red) correspond to the same present in this manuscript throughout Figures 6–10. See Section 4.3 for interpretation. Seismic profiles were modified from Camerlenghi et al. (2020—fig. 4b), Gambino et al. (2022—fig. 2) and Micallef et al. (2018—fig. 1).

TABLE 1 Correlation between the seismic units from other studies and ours, with the inferred chrono-stratigraphy.

Age/Units	Micallef et al. (2018)	Camerlenghi et al. (2020)	Gambino et al. (2021), Gambino et al. (2022)	This study (2023)
Miocene	Pre-MESC	Pre-MESC	Pre-MES	BH/Acoustic Basement
	Unit 3a + 3b + 3c	MU + UU	MES	
Pliocene	Unit 1	PQc	PQ1	Unit A
		PQb		Unit B
Pleistocene–Holocene		PQa	PQ2	Unit C

when possible. The main reason to analyse and interpret the surface and subsurface data independently is to find out to what extent sedimentary and tectonic processes can be deduced from the different data sets and analysis methods. This approach aims to verify whether it is possible to reconstruct the subsurface history based on the surface alone, given that bathymetry is a broader and cheaper survey option. The comparison between the two interpretations is presented in the discussion.

4.1 | Morphology

The integration of bathymetry and surface-derived attributes indicates different types of morphology within the area of interest (Figures 4 and 5): (1) topographic highs (main topographic high and isolated topographic highs), (2) erosional features (channels and scars), (3) depositional features (sediment waves and basins) and (4) tectonic features (faults).

4.1.1 | Topographic highs

The topographic high in the central part of the study area is delimited to the north and west by the deviation of drainage paths, and to the west and east through the changes in slope and in the contrast between high and low in the BPI map (Figure 4b). Ranging from 1900 to 2100 m water depth, this topographic high, in the following referred to as Central Area (CA), covers an area of approximately 260 km^2 with an approximate diamond shape in plain view (Figure 5a). From west to east, it has a ramp shape with a crescent slope gradient of 0.8° (120 m decrease in water depth over 9 km). At its highest point in the east/southeast boundary, the seafloor is steeply (16°) inclined to the east (120 m increase in water depth over 420 m).

From BPI and SVF surface attributes (Figure 4b,d), four isolated topographic highs were identified in the direct vicinity of CA. These isolated topographic highs cover a much smaller area than the CA, between 2 and 10 km^2. Three elongated highs referred to as D1, D2 and D3 stand out in the BPI map (Figure 4b) having high values

adjacent to local depressions (low values) and surrounded by flat areas (in yellow on the BPI map, Figure 4b). The elongated features are between 3 and 6 km in length. They show maximum heights of 110, 100 and 160 m with respect to the surrounding seafloor respectively. The fourth isolated high (D4) is better seen in the slope and SVF maps (Figure 4d,f). D4 (Figure 5a) has a circular shape with a diameter of approximately 4 km and a maximum height of 250 m standing out in the BPI attribute map (Figure 4b). In addition, the SVF map highlights small radial ridges of up to 10 m on top of D4 (Figure 4d,f).

4.1.2 | Erosional features

Two main channels bound the CA and are here referred to as C1 and C2 (Figures 4b and 5c). Both channels are connected to one of the major canyon systems that cut the north-eastern Sicilian slope, the Fiumefreddo Valley (Chiocci et al., 2011; Figure 5e). Situated 35 km north of the CA, the major canyon system shows maximum canyon–channel heights of ca. 175 m and ranges from 200 to 2000 m in water depth. As it reaches 2000 m water depth, it bifurcates into C1 to the east and C2 to the north-east–south-west surrounding the CA. Every change in the channels' direction is here referred to as channel bending. Channel C1, the northern boundary of CA, has an overall low sinuosity and channel heights (distance between the thalweg and the channel banks) that range between 80 and 140 m. It can be mapped uninterruptedly for nearly 50 km on the seafloor between 2000 and 2440 m of water depth and presents two well-marked changes in its path direction (Figure 5c, bends B1 and B2). Initially, with a north–south flow connecting to the canyon system from the Fiumefreddo Valley, C1 changes its direction to an east–west flow direction (first channel bend B1 in Figure 5c). In the downslope course of C1, its path changes again towards the NE, followed by a ca. 90° right-hand turn towards SE, referenced here as C1's second bend (B2 in Figure 5c), which follows a straight and narrow path in the same direction. C2 surrounds the eastern and southeastern CA for nearly 40 km with a lower bathymetric expression (i.e. less incised) between 2000 and 2230 m water
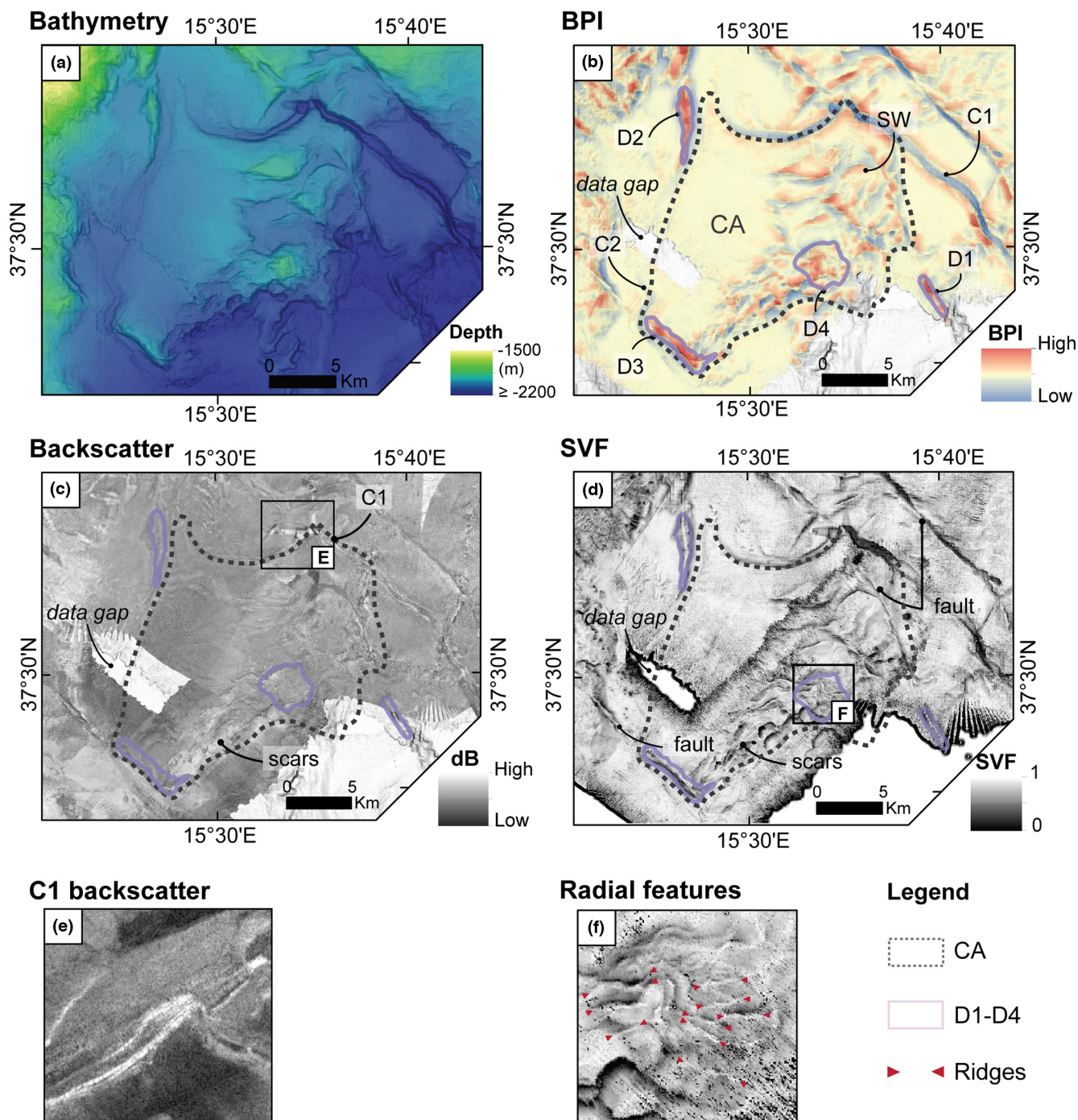
FIGURE 4 Geomorphological interpretation of the Central Area (location in Figure 2). Interpretations were made based on the combined analysis of attribute maps. (a) Uninterpreted bathymetry of the main study area (from Gutscher et al., 2017). (b) Bathymetric position index (BPI) attribute map. (c) Backscatter map. (d) Sky view factor (SVF) attribute map. (e) High-intensity/erosive backscatter pattern of channel C1. (f) Zoom into a circular feature with centric ridges on top (between red arrows). Attributes were calculated for the 30-m-grid bathymetry dataset.

depth. It also shows a narrow, straight path with low sinuosity that runs initially north–south before it reaches the study area. Close to CA it bends and continues in the SW direction (B3 in Figure 5c) before it leaves the southern boundary of our study area in the SE direction. Moreover,

within C2, three ca. 90° channel bends (B4, B5 and B6) can be seen (Figure 5c). C2 presents lower channel height (distance between the thalweg and the channel banks) values than C1, from 15 m to 30 m. Both C1 and C2 have a low-intensity backscatter response in their thalwegs and

a few bright spots and areas over their margins/terraces, near a channel bend (e.g. B2, Figure 4e) or adjacent to isolated highs (as seen near D3) (Figure 4c).

Small amphitheatre-shaped scars (approximately 1 km long) are seen in the CA's south-eastern flank, which, with a slope angle of 16°, is much steeper than the surroundings striking up to 140-m-high breaks of slope (example in Figure 5f). The scars can be delimited by BPI and SVF maps as elevated areas and sharp edges respectively (Figure 4b,d). Nearly 20 scars are lined up with an SW–NE trend and thus perpendicular to the maximum slope gradient (Figure 5c). They cover an area of 2×10 km and nearly all are adjacent to local seafloor depressions (BPI low values, Figure 4b). In the backscatter, the depressions appear as high-intensity backscatter areas or bright areas (Figure 4c), which indicates the lack of hemipelagic deposits compared to the surrounding seafloor.

4.1.3 | Depositional features

Five elongated and parallel lineaments are seen in the BPI and SVF maps as alternated high and low features (Figure 4b,d, and outlined in Figure 5b). These undulated features are interpreted as sediment waves and cover an area of approximately 24km^2 on the seafloor, on the northeastern flank of the CA. Ranging from 2000 to 2200 m in water depth, their wavelengths are approximately 1 km, with a wave height of 60 m. These features show no significant variations in the backscatter map (Figure 4c).

Basins are defined by the relatively flat and smooth semi-circular areas in the bathymetry and the attributes maps. In BPI maps, basins correspond to yellow areas (values close to 0) (Figure 4b, location in Figure 5b). They are mainly located in between higher structures. The main minibasin within the CA has an area of approximately 123km^2 (Figure 5b). It is characterized by low backscatter indicating smooth and homogeneous sediment deposition (Figure 4c, location in Figure 5b).

4.1.4 | Tectonic features (faults)

Numerous morphological lineaments on the seafloor are aligned over distances of several kilometres. These lineaments consist of vertical offsets of up to 40 m with steep slopes of approximately 20°. These morphological characteristics suggest that these slope breaks represent faults (Figures 4d and 5d). Offsets of other morphological features, such as channels and ridges (Figure 5g), along these lineaments suggest that they are two right-lateral NE–SW-trending strike-slip faults that bound the CA. The southern strike-slip fault has been previously described

as the North Alfeo Fault (NAF) (Gutscher et al., 2015; Gutscher et al., 2017). Two of the isolated highs, D1 and D3, are adjacent to these faults (D1 to the north faulting bound and D3 to the NAF), while D2 and D4 are in between these fault systems. The horizontal 500 m offset of ridge NW of C1's second bend (B2) (Figure 5d,g) is the most prominent example of offsets along the faults. Moreover, this ridge-like structure and the topographic high of D1 coincide with the NE fault bends (Figure 5d). Both the offset and the morphological change along the fault support the right-lateral shear sense of the north-bounding fault. Yet, the NAF right-lateral motion is proven by Gutscher et al. (2015), Gutscher et al. (2017) and Gutscher et al. (2019).

## 4.2 | Stratigraphy

4.2.1 | Basement highs

In the following, we refer to the acoustic basement as the part of the seismic data into which the acoustic signal no longer penetrates, which is source-dependent. In the seismic data analysed, the acoustic basement top is generally marked by a moderate- to high-amplitude locally discontinuous boundary, referred to as the H0 horizon. Below this horizon, the acoustic basement appears in the seismic data as low amplitude with chaotic to transparent facies (Figure 6a).

The acoustic basement reaches the seafloor or closely approaches it in five locations, which we here refer to as basement highs. The five basement highs differ in size and shape: (i) a wide area of approximately ca. 6 km width and 700 ms thickness two-way travel time (TWT), with a crescent ramp shape towards SE (Figure 6a), (ii–iv) three narrow vertical features that are between 700 and 1200 m wide, and 900 ms and 700 ms TWT thick (Figure 7a,b,c) and (v) a large feature of 2.5 km wide and 1000 ms TWT thick (Figure 7d). The basement highs match the CA (i) and the isolated topographic highs (ii–v) identified in the bathymetry and surface attributes (Section 4.1), therefore we use the same naming convention as for the bathymetric description, that is, CA (i), D1 (ii), D2 (iii), D3 (iv) and D4 (v) (Figures 5a and 7). D4 is located within the Central Area making it difficult to distinguish the two features in the seismic data.
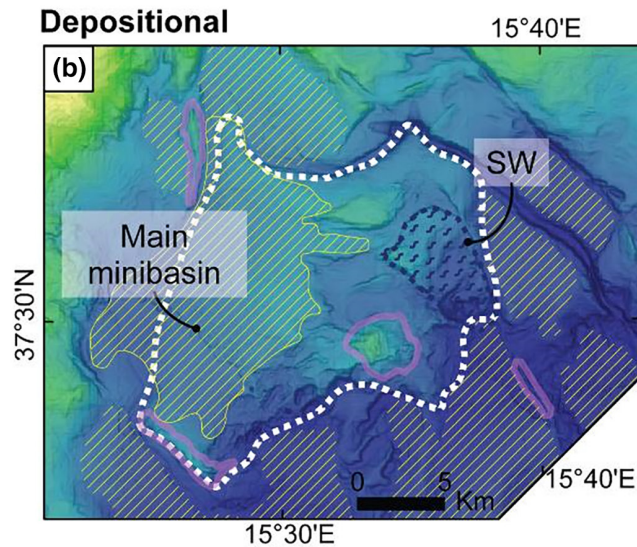
4.2.2 | Unit A

Above the acoustic basement, Unit A has low-amplitude seismic facies with parallel tilted reflectors that dip away from the CA (e.g. SE, Figure 6a). Unit A comprises a
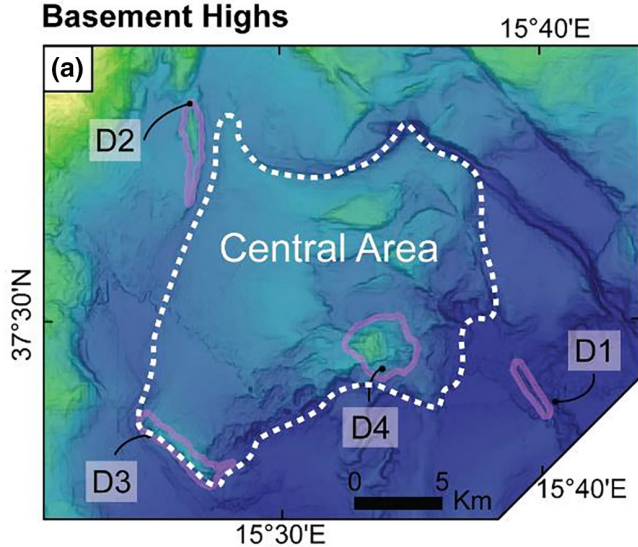
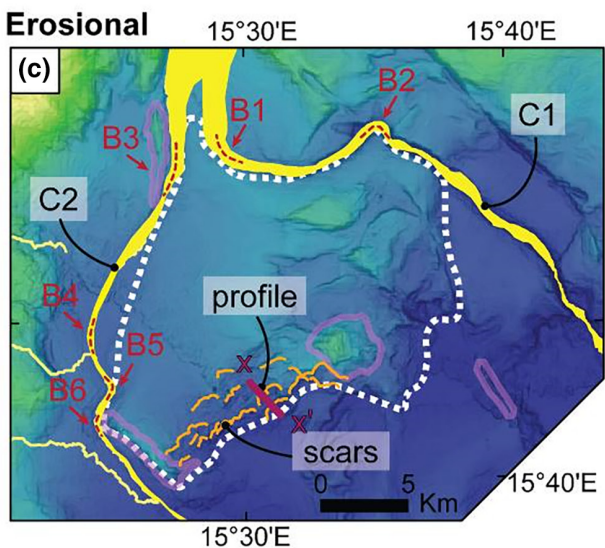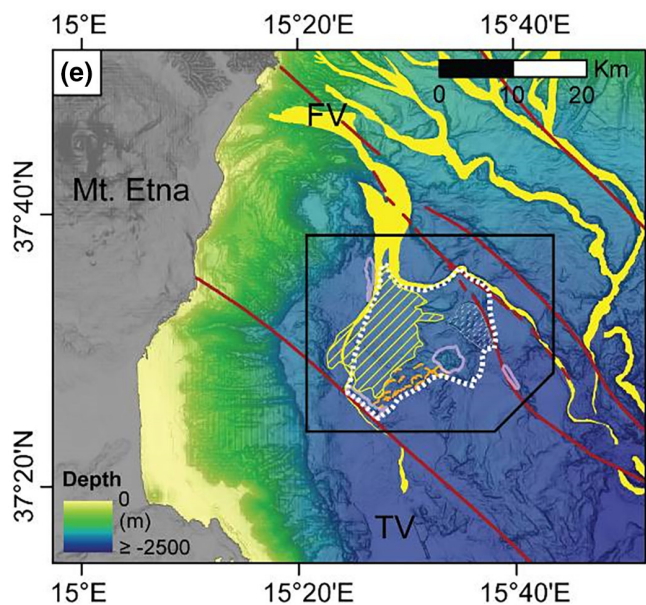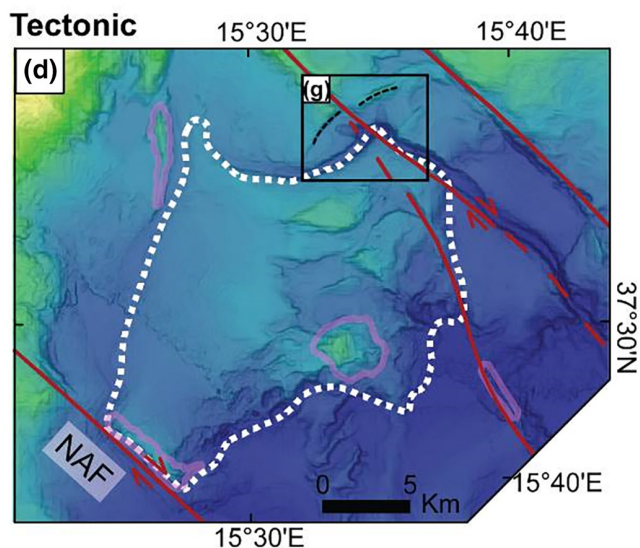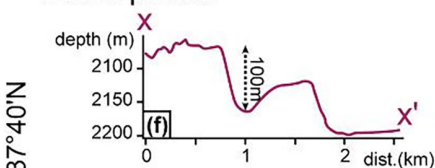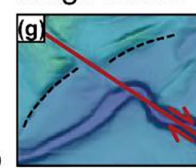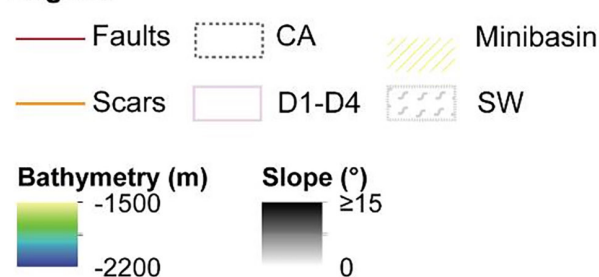**FIGURE 5** Geomorphological interpretation of the Central Area (location in Figures 2 and 5e) based on the attribute maps in Figure 4. (a) Interpretation of the main topographic/basement high in white (the Central Area) and the isolated topographic/basement high features in pink (D1–D4). (b) Interpretation of the depositional features highlighting the Main Minibasin and the sediment waves field. (c) Interpretation for the erosional features of head scarps (profile on Figure 5f), and channels C1 and C2 with their respective channels bend (B1–B6) marking changes in the channels' paths. (d) Interpretation of the tectonic features, main faults. (e) Combined view of all the interpretations presented before. (f) Profile perpendicular to scars seen on Figure 5c. (g) Zoom in on the vertical offset of a linear ridge on the seafloor seen in Figure 5d. FV, Fiumefreddo Valley; TV, Turbidite Valley.
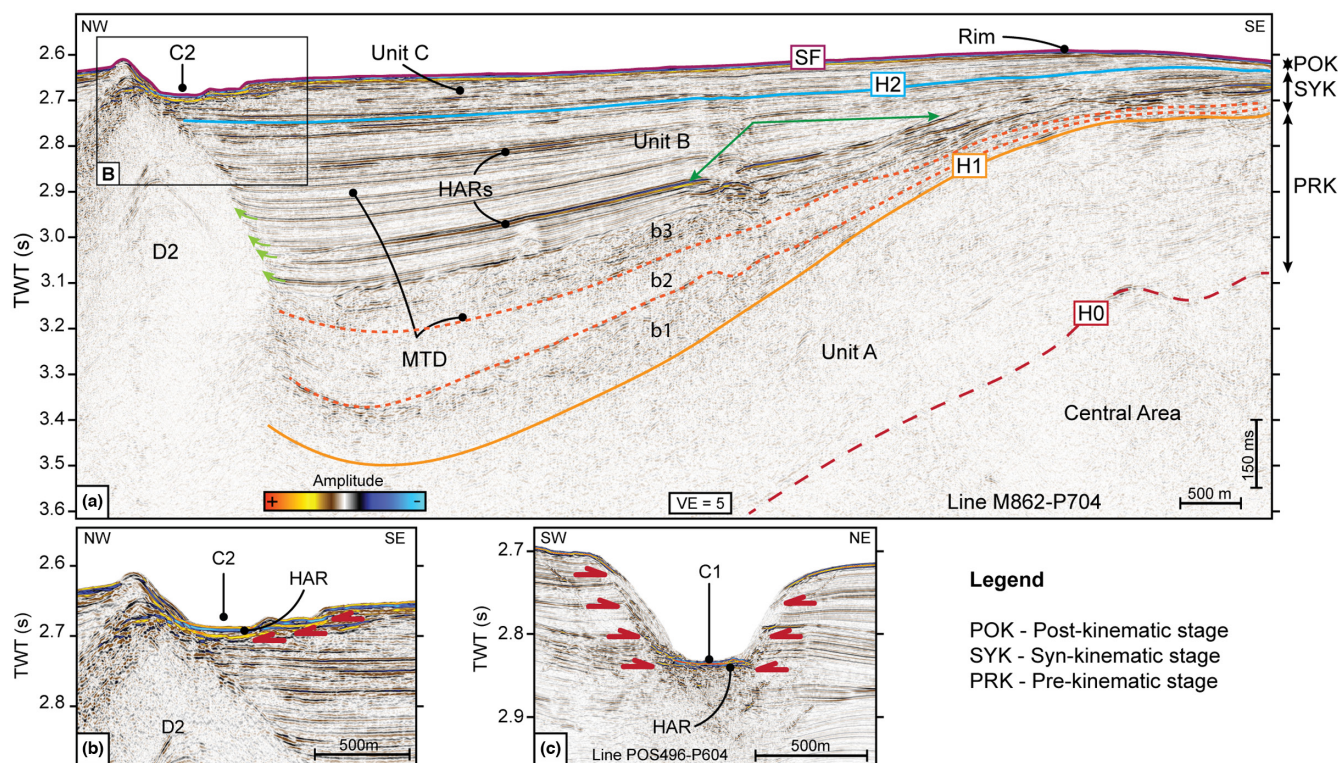

FIGURE 6 Cross-section of the Main Minibasin through the basement high features, later referred to as D2 and Central Area (location Figure 2). (a) Sagging basin with three main units. Unit A, the pre-kinematic stage with tilted reflectors, no lateral variation in thickness and concordant to H0 top boundary. Unit B, the syn-kinematic stage with lateral variation in thickness due to uplift (green arrow), MTDs in the depocentre, discordant terminations and cut-off reflectors (light green arrows) by diapir D2. Unit C, the post-kinematic stage with onlap termination, no lateral variation in thickness due to uplift. On the seafloor (SF), a rim feature and the erosional surface for channel C2 can be seen. (b) and (c) Channel C2 and C1 cross-sections with high-amplitude reflectors (HAR) at their thalwegs and truncated surface/onlapping reflectors shown as red arrows. VE, vertical exaggeration.

sediment package with a thickness of approximately 330 ms (TWT), having no or minimal lateral change in thickness across the area of interest. This unit is limited downward by the H0 horizon where it is concordant and upward by the H1 horizon discontinuity.

4.2.3 | Unit B

The overlying unit, Unit B, presents moderate- to high-amplitude seismic facies with parallel reflectors that pinch out towards the shallower parts of the basement highs (e.g. SE, Figure 6a) and/or are cut off by the narrow outcropping

of the D1, D2, D3 or D4 feature, depending on its location (e.g. NW, Figures 6a and 7). Unit B is bounded downward and upward by discontinuities H1 and H2 horizons respectively. Within this unit, thick high-amplitude reflectors (HARs) deposited at the depocentre are seen thinning towards the southeast (e.g. Figure 6a). Moreover, truncated reflectors and other significant lateral changes in thickness, from 140 ms (TWT) at the top of the basement highs (SE, Figure 6a) to 650 ms (TWT) in the depocentres (NW, Figure 6a), are observed. Locally, chaotic low-amplitude seismic facies are seen at several depth intervals near the flanks of D1 to D4, in between parallel strata, at the base of this unit or minibasin depocentres, and in the vicinity of fault planes (Figures 6a
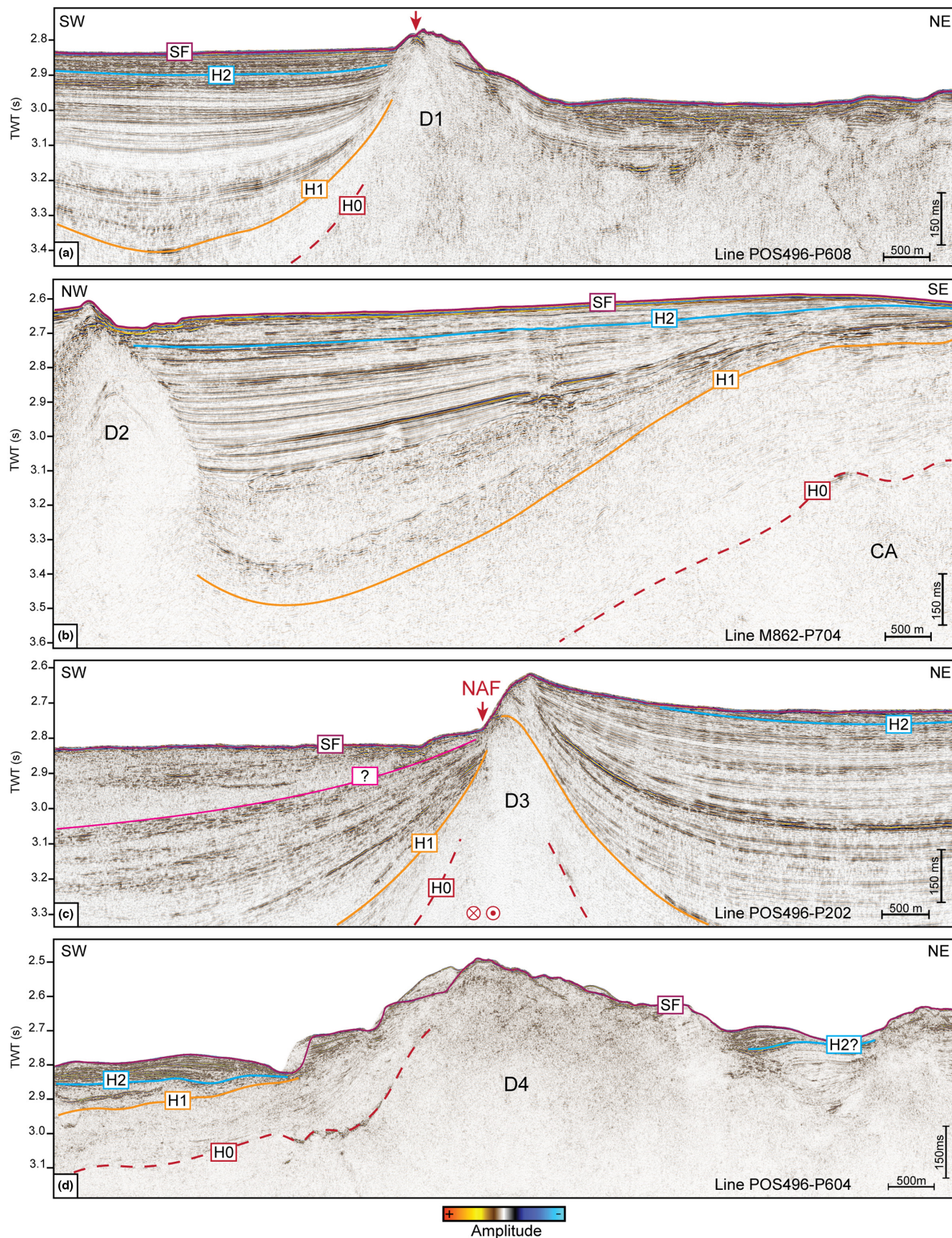
FIGURE 7   Cross-section from the isolated topographic/basement highs in the study area. (a) Diapir D1 formed adjacent a strike-slip fault. (b) Diapir D2. (c) Diapir D3 formed adjacent to the North Alfeo Fault (NAF). (d) Diapir D4. D1 and D3 are adjacent to the main strike-slip faults that bound the Central Area, while D2 and D4 are in between the same fault systems. Red arrows indicate the seafloor expression of the fault systems. Locations in Figure 2. VE, vertical exaggeration.

FIGURE 8 Cross-section from diapir D3, adjacent to the North Alfeo fault system (NAF, red arrow), cutting off the minibasin deposits. Reflector terminations near the seafloor are tilted (black arrows) and may indicate an active uplift. Within the minibasin, thinning strata, high-amplitude reflectors (HARs) and mass transport deposits (MTD) are seen near the diapir flanks. Location in Figure 2. VE, vertical exaggeration.
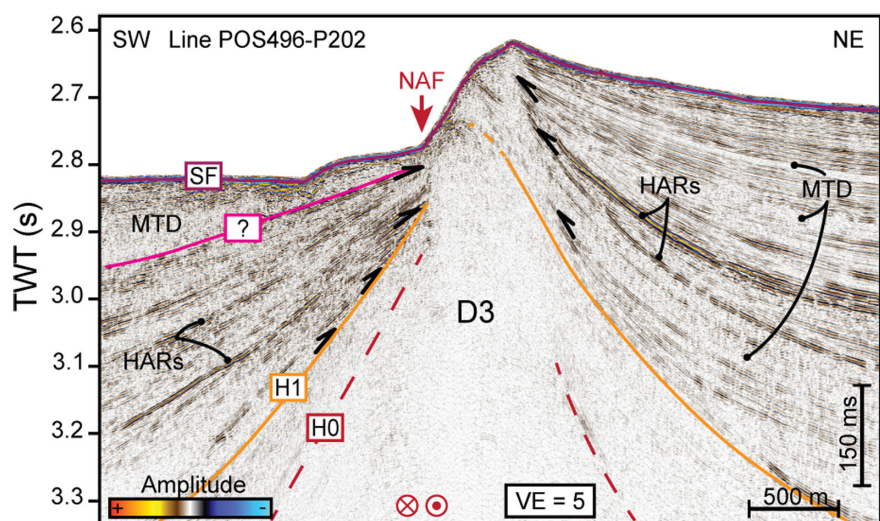

FIGURE 9 Buried contourite features (CF) with a sequence of mounts and moats. The contourite features are located SW of Diapir D4 within Unit B (syn-kinematic stage) and migrate upslope of the tilted Unit A. Unit B can be further subdivided into sub-units b1, b2 and b3. Decreasing dipping angles from b1 to b3 indicate different depositional stages and consequently uplifting phases. BH/AB, basement high/acoustic basement; VE, vertical exaggeration.
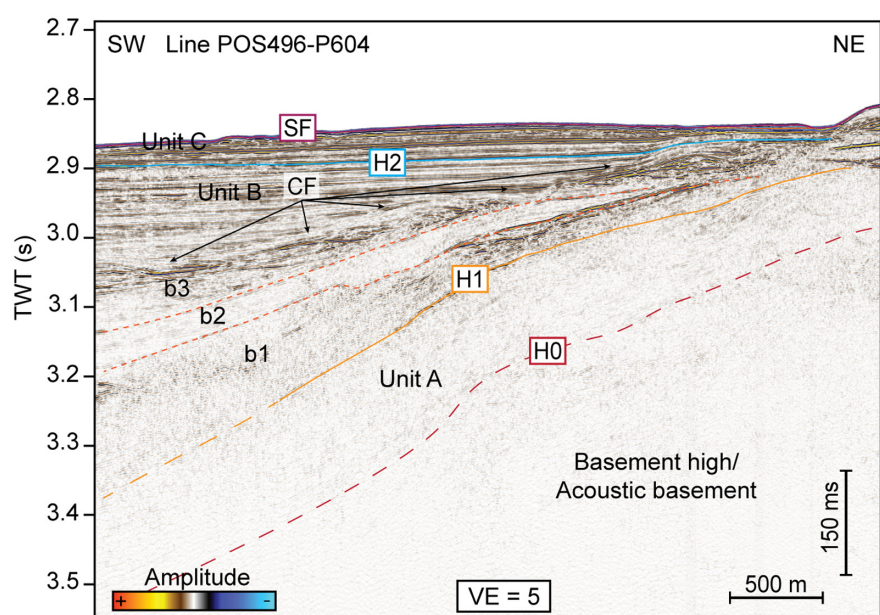
and 8). In some places, this unit can be further subdivided into three sub-units (b1, b2 and b3) that have distinct decreasing dipping reflector angles, facies and amplitudes (Figure 9). The sub-unit b1 presents moderate amplitude with chaotic to discontinuous facies and is marked locally by a strong top boundary. Sub-unit b2 is mainly characterized by low-amplitude plan parallel reflectors that pinch out towards the basement high or Central Area. Last, the sub-unit b3 is marked by moderate- to high-amplitude reflectors that onlap and/or pinch out towards the CA. In this unit, upslope wavy features can be seen locally (Figure 9).

4.2.4 | Unit C

The uppermost unit, Unit C, has parallel and continuous reflectors and shows onlap. It is bounded downward by

the H2 discontinuity and upward by the seafloor (SF). Locally, truncated reflectors are seen marking the C1 and C2 channels (Figure 6b,c). No pinch-out or truncated sediments are observed on the flanks of D1-D4 features. With thickness that ranges between 46 and 75 ms (TWT), the lateral change in thickness within Unit C follows the seafloor morphology. A slightly elevated seafloor above the SE basement high's flank is described as a raised bathymetric rim (Figure 6a, towards the SE).

4.2.5 | Internal features

Undulating features are seen at two separate locations on opposite sides of the basement high D4 (Figures 9 and 10, location in Figure 2). Towards the southwest of D4, buried undulating features within Unit B, more precisely within
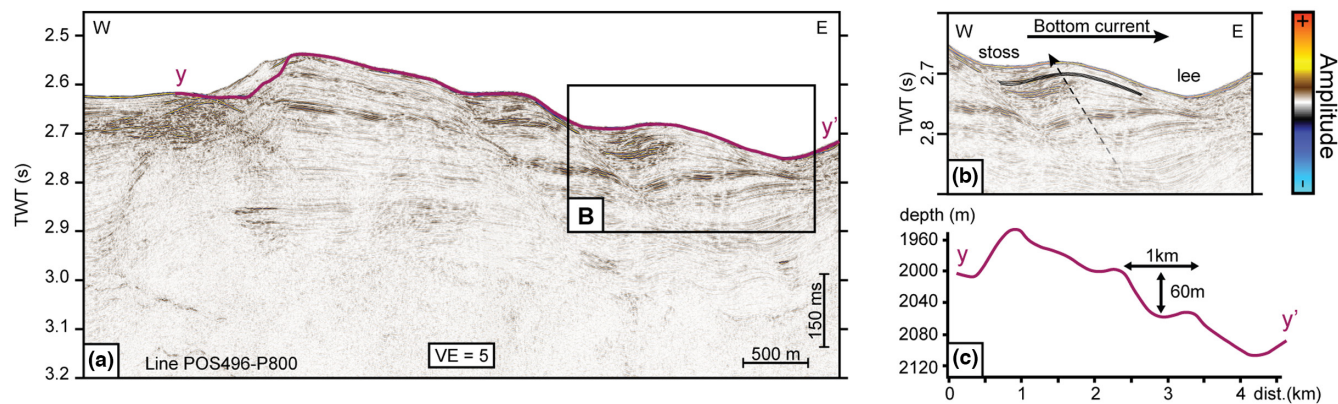
FIGURE 10 (a) Sediment waves on the seafloor, NE of diapir D4. (b) The sediment waves present a thicker depositional stoss side on the west and a pinched/erosional lee side on the east, as seen on lee-wave models. The waves show a western crest migration (dotted arrow) and a bottom current direction that can be inferred as W–E flow (bold arrow). (c) A bathymetric profile from the sediment waves shows a wavelength of 1 km and wave heights of 60 m. Location in Figure 2.

sub-unit b3, are seen upslope of the tilted strata, from 2.9 s to 3.05 s (TWT) towards NE (Figure 9). The undulated features stack towards SW–NE (Figure 9), resembling sediment waves or an upslope sequence of moats and drifts. Northeast of D4, a wavy sediment package of approximately 400 ms TWT thickness, has a topographic expression at the seabed (undulated features in Section 4.1) covering a small area (ca. 24 km^2) within the CA with 1 km wavelengths and 60 m wave height. Although the seismic profiles only cover the area partially, it is possible to observe steeper western-facing flanks with thicker and higher-amplitude reflectors, and eastern-facing flanks with thinner low-amplitude reflectors (Figure 10). This distinction in the reflector spacing and terminations are typical for sediment waves (Wynn & Stow, 2002).

4.3 | Inferred chrono-stratigraphy

Through seismic correlation (seismic units and facies) (Figure 3), it is possible to define a relative chrono-stratigraphy based on other seismic studies for the Ionian Basin, although there is no well control for the upper Calabrian accretionary wedge that would provide absolute ages. A summary of the chrono-stratigraphic correlation can be found in Table 1.

Two of the most extensively described units in the literature are the Pre-Messinian and the Messinian Unit, which can be subdivided according to the evaporite composition. The Pre-Messinian is described by its lateral continuity, high-amplitude and general sub-parallel reflectors slightly tilted and offset by sub-vertical faults, as well as flower and pop-up structures (Camerlenghi et al., 2020). Camerlenghi et al. (2020) and Micallef et al. (2018) divide the Messinian unit into three sub-units going from a highly reflective, discontinuous unit (3c or Lower Unit) to

an intermediate reflector-less unit with a basin-fill geometry (3b or Mobile Unit) to a discontinuous-to-continuous, highly reflective and mostly deformed upper unit (3a or Upper Unit). Gambino et al. (2021), Gambino et al. (2022) and Gambino (2022) summed up this unit by describing it as having an upper chaotic portion, a layered, parallel and continuous middle portion, and a lower transparent level. This resembles the basement high facies in this study.

Locally, there is a chaotic, discontinuous and variably transparent unit on top of the Messinian salinity crisis (MSC) evaporites (Camerlenghi et al., 2020). This has been interpreted to consist of the sediments eroded from the Mediterranean continental slope during low sea levels in the time of the MSC (Camerlenghi et al., 2020). Unit 2 of Micallef, Camerlenghi, et al. (2018) is referred to as the Zanclean Megaflood Deposits or Complex Unit by Camerlenghi et al. (2020) and marks the Miocene–Pliocene transition. We do not observe this unit in our study area as it is limited to the foot slope along the Malta Escarpment.

The various studies subdivide the Pliocene–Quaternary deposits into different subdivisions. Unit 1 is described as high-amplitude, continuous, parallel to sub-parallel reflectors that are linked to the pelagics, contourites (sediment waves in the shallower section) and turbidites from this geological time (Micallef, Camerlenghi, et al., 2018). Camerlenghi et al. (2020) identified three sub-units in the Ionian Basin: PQc, PQb and PQa. PQc, the lowest sub-unit, has low reflection strength with lateral reflectivity changes. At the base of PQc, a thin irregular layer with poor lateral continuity and higher amplitude can be seen. PQb is composed of sub-parallel and laterally continuous high-amplitude reflectors with a well-marked transition to the upper unit, PQa, that presents parallel and laterally continuous reflectors with moderate amplitude (Camerlenghi et al., 2020). Gambino et al. (2021) and Gambino et al. (2022), in turn, describe a PQ1 unit characterized

by a transparent level and a PQ2 upper unit with high-amplitude, high-frequency horizontal, parallel and laterally continuous reflectors.

Our units (A, B and C) correspond to the units PQc, PQb and PQa from Camerlenghi et al. (2020) respectively. Unit A and PQc have similar seismic facies and are conformably folded with the underlying Messinian unit. It is separated from the upper unit by a marked unconformity, here the H0 horizon. Unit B and Unit PQb are characterized by the same parallel, high-amplitude and lateral continuous reflectors. Unit C and PQa show moderate-amplitude and lateral continuous reflectors that include sediment waves as also seen in Unit 1 of Micallef, Camerlenghi, et al. (2018) and Unit PQ2 of Gambino et al. (2021) and Gambino et al. (2022).

5 | DISCUSSION

Several morphological and geomorphological classifications were proposed for the Ionian Basin on a basin-wide scale (e.g. Gutscher et al., 2015; Gutscher et al., 2017). Here, we take a close look at the sedimentary processes and tectonics within the study area to understand what they can reveal about the area's history of vertical movement. We discuss the individual changes observed in the seabed and subsurface and how they point to vertical movement over time in the study area. Moreover, we combine all the evidence to suggest two different uplift origins and timing based on the discussed features that can serve as proxies in assessing vertical movement evolution in a broad sense.

5.1 | Changes in the sedimentary system and their relation to vertical movement

5.1.1 | Channels

The main study area is surrounded by channels C1 and C2 (Figure 5c). The upslope connection between channels C1 and C2 and the contributing canyons on the shelf, as seen in the bathymetry, suggest that the channels are formed by gravity-driven currents that transport clastic sediment into the abyssal plain.

While the slope canyons that connect C1 and C2 to the shelf seem to still be active, having high backscatter values, channels C1 and C2 present mainly low backscatter intensity values (Figure 4c). This change from high to low backscatter can have different reasons, for example, either the lower parts of the channel are currently inactive and filled with fine sediments, or the decrease in the slope

causes a lower energy environment that allows deposition of fine-grained material. However, it cannot be ruled out that backscatter is reduced by imperfect imaging due to the steep channel flanks that cause less energy to be reflected back to the hydroacoustic receivers. This is supported by the fact that the seismic data show high-amplitude seafloor reflectors in the thalwegs of the channels suggesting that C1 and C2 are currently active (Figure 6b,c) at least within the seismic resolution (5 m vertically).

Uncharacteristically, both channels show sharp bends in their downslope direction (Figure 5c). The observed bends are unlike meanders as they are single changes in direction and can be almost rectangular, that is, up to 90°. In one extreme case (B1 towards B2, in C1), the bend causes an almost 150° change in flow direction compared to its dominant direction prior to reaching the study area (Figure 5c). The more pronounced bends B1 and B2 are at the northern boundary of the CA, that is, in the upslope part of the channels, while the less incised bends B3 and B4–B6 are further downslope in the vicinity of the topographic highs D2 and D3 respectively.

This change in direction in overall low sinuosity channels can be explained by the forced deformation of the channels after encountering a barrier that evolved in the seabed, preventing the channel from following its original single and straight downward direction. Other explanations for the channel's high curvature bends are changes in sediment delivery (deposition and/or erosion). However, no point-bar deposits or lateral migration due to erosion is seen in channels C1 and C2, suggesting that a bend due to sediment delivery change is unlikely. On the other hand, high-curvature bends have been seen previously around complex topography environments (e.g. in vertical movement or rapidly deforming settings) that are able to localize channels' pathways (Covault et al., 2020). Even small topographic changes are sufficient to shift channel system locations (Covault et al., 2020). Hence, we conclude that the uplift of the Central Area, D2 and D3 formed topographic barriers that caused the channels to change directions.

With that said, the changes in channel morphology and direction can be used as relative time constraints for vertical movement. From the morphological evidence, we infer that (i) at the point in time when no obstacles were in its way, the canyon–channel system went through the Ionian Basin, crossing the CA until reaching the Turbidite Valley and other lower areas forming minibasins (Figure 11a); (ii) due to the active uplift of the CA, branches of the canyon system (proto unconfined C1 and C2) formed to avoid the now elevated area and fill in what we referrer here as the Main Minibasin with coarse sediments that are translated into HARs typically seen in sand lobes (Figures 11b, 6a and 8); (iii) with the continuous rising of the CA, a confined C1 is formed and forced to deviate from
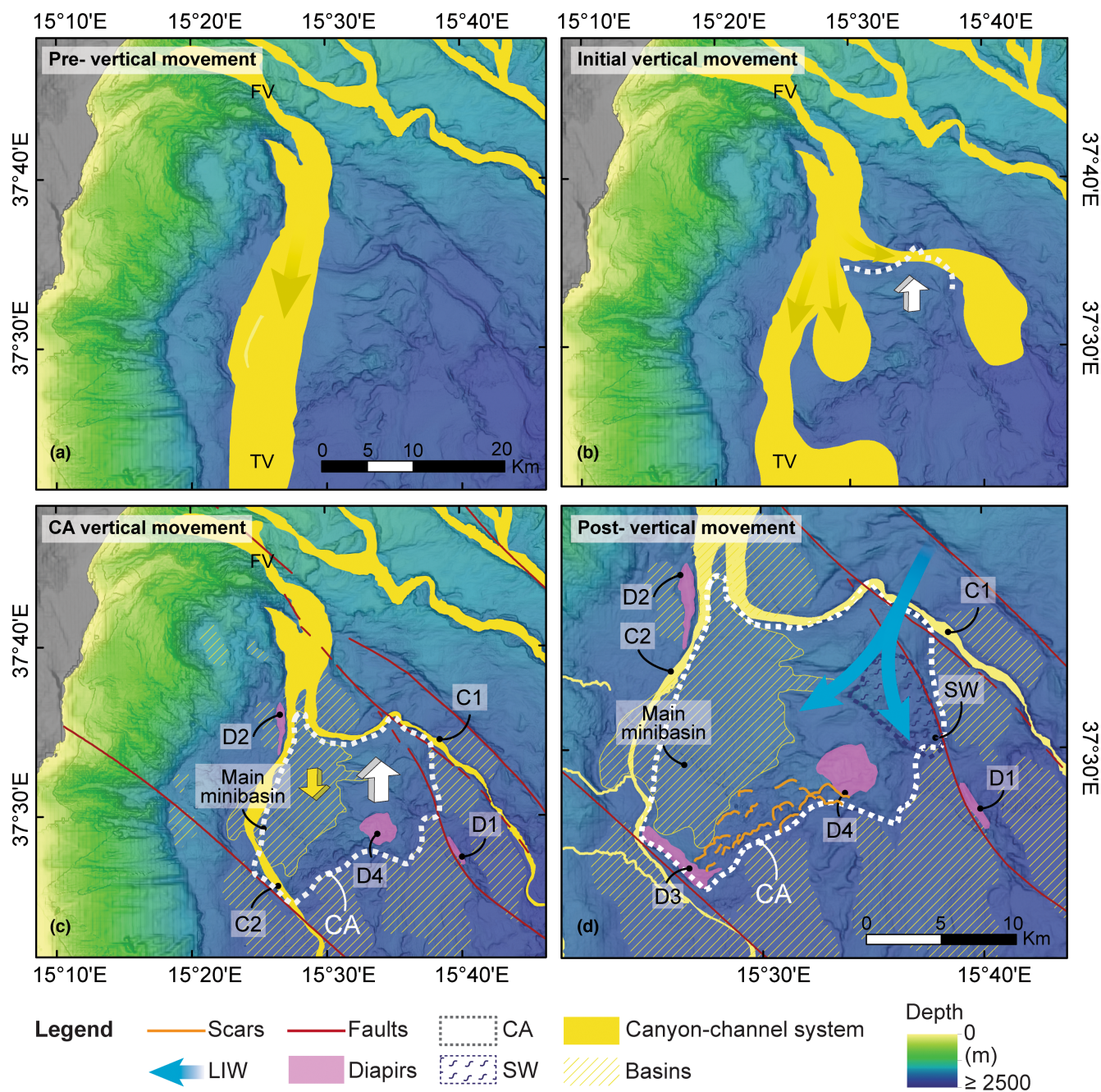
FIGURE 11 Reconstruction of the sedimentary processes active on the basin before, during and after the vertical movement of the Central Area and the diapirs D1–D4. This model is based on the interpretation of the geomorphological proxies, especially the channels' deviations. (a) Pre-vertical movement: predicted path for the canyon system from the Fiumefreddo Valley (FV) in a pre-elevated or plain topography, connecting the FV to the Turbidite Valley (TV). (b) Initial vertical movement: the vertical movement starts at the north boundary of the Central Area (dotted white line and bold white arrow). The canyon system divides into a smaller channel branch (yellow arrows), channel C1, which is forced to deviate from the topographic high. (c) CA vertical movement: the continuous vertical movement of the Central Area (bold white arrow) forms accommodation space for the formation of the Main Minibasin that is filled by the canyon–channel system and subsides with the weight of the sediments (bold yellow arrow) and in turn uplifts D1, D2 and D4. The uplift of the D2 channelizes the FV system forming channel C2. C2 is deviated due to the uplift of the Central Area. (d) Post-vertical movement: lastly, D3 is uplifted deviating channel C2 once more, forming two 90° path deviations surrounding D3. The newly formed topographic highs improve the interaction between bottom currents and the seafloor. The LIW is forced to deviate from D4 and as a result, sediment waves (SW) are seen on the seafloor.

the northern uplifted CA (B1 and B2 Figures 5c and 11b); (iv) later, with the rise of D2, C2 became confined and was forced to deviate from the CA (B3 and B4 Figures 5c and 11c); (iv) last, D3 uplifted and forced C2 to deviate around its positive relief, forming the other bends (B5 and B6 Figures 5c and 11d, current seafloor).

5.1.2 | Slope failure

The seismic data show chaotic seismic facies at several depth intervals of Unit B (Figures 6a and 8). Such seismic facies within otherwise stratified sediments are indicative of submarine slope failures commonly termed mass transport deposits (MTDs). MTDs are located in the small basin depocentre (in the Central Area) and near the flanks of D1 to D4 (Figures 6a and 8). While the sparse seismic data coverage does not allow us to pinpoint the origin of these MTDs, this observation clearly shows that parts of the region are prone to slope failure although it is beyond the continental slope, where MTDs are common. Identification of submarine landslides is a good indicator for recognizing active uplifting and quantifying structural growth (Doughty-Jones et al., 2019).

The bathymetric amphitheatre-shaped SW–NE scars described in Section 4.1 are limited to the steepest flank of the CA (Figures 5c and 4a) and are interpreted here as the headwalls of several small slope failures. An erosional origin of the scarps by bottom currents, similar to 'honeycomb' features or moats (e.g. Hernández-Molina et al., 2022; Sun et al., 2017), can be discarded because (i) the features are not circular as formed by eddies; (ii) they do not show repeated erosion and infill as the 'honeycomb' features formed by eddies; and (iii) the scarp throughs are not connected, as expected in moats from the bottom current reworking.

Therefore, we interpret these breaks of slope as headwalls. This is consistent with high-amplitude backscatter at the foot of the breaks of the slope. We interpret the absence of hemipelagic sediments (low backscatter) as a result of sediment removal due to small slope failure. In the study area, the scarps on the SE flank of the Central Area are the only bathymetric evidence of recent slope failures. This flank is the steepest part of our study area (up to 16°) and is bounded by two isolated topographically high features (D3 and D4, Figure 5a,c).

In our study area, the two different indicators for slope failure: MTDs in the seismic data and the headwalls in the bathymetric data are possibly caused by a final oversteepening of the slopes (Figure 11d). We propose that the uplift of the Central Area and associated tilting of the seafloor pre-conditioned the area for slope failure. However, it was the posterior deformation or uplift of D3 and D4 that finally triggered the landslides and resulted in the scarps and depressions observed today.

5.1.3 | Bottom current features

Contourite drifts are widely recognized by their elongated mounded shape and adjacent erosional/non-depositional features or moats, along which the flow focuses (Rebesco et al., 2014). In the study area, mounded and undulating features are seen in two different locations.

First, Unit B hosts buried elongated mounded features with adjacent erosive surfaces that migrate upslope sub-units b1 and b2, on top of tilted Unit A (Figure 9). The erosive features, in sub-unit b3, cut through the sediment beneath and represent small-scale moats. The succession of elongated mounds and moats is a morphology typical for contourite drifts formed by reworked sediment (e.g. Hernández-Molina et al., 2022). The sequence of mounded features in the study area is here interpreted to be the result of bottom current and seafloor interaction.

Bottom currents form drifts, moats and sediment waves by interacting and reworking the sediments on the seabed as they hit an obstacle. For this reason, the onset, as well as migration of these features, document the initiation and ongoing rise of seafloor structures, making contouritic features suitable proxies for uplift (Schattner et al., 2018). In the study area, buried moats and mounds are only present in Unit B (not below) suggesting that no bottom current–seafloor interaction existed prior to the deposition of Unit B. As the buried contouritic features migrate upslope a deformed and tilted overlying unit, we propose that bottom current–seafloor interaction is a result of seabed uplift. The uplift of the CA promoted the interaction between bottom currents and the seafloor, which in response forced the migration of the current core upslope forming the sequence of contouritic features within Unit B (Figure 9).

Second, within the CA, the seafloor morphology reveals undulating features on the seafloor. As described in Sections 4.1 and 4.2, these features fall under the definition of sediment waves as 'large-scale undulating depositional bedforms that are generated beneath a current flowing at, or close to the seafloor' (Wynn & Stow, 2002). By definition, sediment waves can be generated by bottom currents or gravity-driven currents (Wynn & Stow, 2002). According to the scheme proposed by Rebesco et al. (2021), sediment waves caused by turbidity currents typically (i) occur inside channels and channel levees, (ii) are parallel to the regional slope, (iii) tend to decrease in size downslope and (iv) progressively thin downslope. The sediment waves that we observe in the CA occur on the plane top of a topographic high and are oriented NW–SE while the regional slope is W–E. Due to limited seismic coverage, the decrease in size is not clear. Nevertheless, based on these observations, we exclude a turbidity origin for the sediment waves in this study area and bottom currents are a much more likely origin. This is consistent with the presence of bottom current-related sediment waves in other areas of

the upper Calabrian ridge (Marani et al., 1993; Rebesco et al., 2021).

The sediment waves in the study area only occupy a small area and have distinct depositional and erosional patterns on their lee and stoss sides (Section 4.2, internal features). This combination points to the interaction between weak stratified bottom currents and irregular topography which generates internal lee waves (Flood, 1988). Sediment waves formed by lee waves are usually oblique to the flow and are distributed in very small-wave fields of one or two waves only (Blumsack, 1993). Also, these internal lee waves trigger higher bottom current flow velocities on the down flanks (lee side) rather than the up-current flanks (stoss side). Such difference in flow velocity favours the deposition on the stoss side and consequently, up-current migration. As seen in the seafloor sediment wave in the study area, this pattern is translated into (i) thin or eroded/truncated low-amplitude reflectors on the lee side (east flank, Figure 10) due to higher flow velocities, and (ii) thick depositional high-amplitude reflectors on the stoss side (west flank, Figure 10), with thicker and spaced reflectors due to the low velocities of the bottom currents. These observations confirm the local bottom current interaction origin of the sediment waves. Yet, the configuration of the sediment waves (lee and stoss sides) also indicates a flow direction from west to east and an up-current wave crest migration, that is, the crest of the waves grows in the opposite direction of the bottom current flow (Figure 10, dotted arrow).

Interestingly, the Levantine intermediate water (LIW) is the main bottom current within the study area and flows from north to south along the Sicilian continental rise (Section 2.2). To understand the formation of sediment waves under a W–E flow, we have to take into consideration bottom current flow direction variations, such as flow deviations surrounding topography changes.

The very localized and small area in which the sediment waves occur on the seafloor (Figure 10) is within the CA and north of D4 (Figure 5b). Both CA and D4 are topographic highs and can therefore modify the bottom currents' paths and force their interaction with the raised seabed, as topographic barriers on the seafloor are known to change the ocean bottom currents' path, magnitude and velocity (Schattner et al., 2018). It is likely that the LIW changes its flow direction from southward to western-eastward as it encounters the topographic highs of CA and D4. We propose that they forced the LIW to deviate or bypass the topographic highs by changing its direction by ca. 90° and turning it momentarily towards the west–east (Figure 11d). Since the topography is higher towards the east due to the Central Area vertical movement, only the eastward ramification from LIW interacts and reworks the seafloor. The fact that the sediment waves occur only next to these obstacles indicates that they are genetically related.

Because the first occurrence of sediment waves is known in a relative timeframe from the seismic data, it is possible to establish the relative timing. First, the CA rise favoured the interaction between the bottom currents and the seafloor causing the mound and moat structures to form at the west flank of CA. Then, D4 uplifted forming a barrier for the southward flowing bottom current forcing its deviation and forming the sediment waves seen on the seafloor. Therefore, the sediment waves could only be formed after D4 vertical movement started and became an obstacle to the N–S natural flow direction of the bottom currents. Thus, the thickness of the sediment wave package adjacent to D4 should be a proxy for its minimum time of origin, that is, it should be at least as old as the deepest contouritic feature/sediment wave seen on the stratigraphy. As the top of the deepest sediment waves is 400 ms (TWT) lower than the present seafloor, the uplift of D4 seems to be of this order of magnitude.

5.1.4 | Sedimentary depocentres

The study area hosts several sedimentary basins in between topographic highs, as well as downslope from the canyon systems along the Sicilian continental slope (Figure 5b). In the following, we refer to the basin that is surrounded by the topographic highs CA, D2, D3 and D4 (Figure 5a,b) and the two main strike-slip faults in the study area as the Main Minibasin. Stratigraphically, we divide the Main Minibasin into basement highs and the sedimentary units A, B and C (Figure 6a).

The internal seismic configuration of sedimentary basins provides information on changes in the environment, sediment transport processes and tectonics (faults) (Chapman, 1983). These are reflected in thickness, contact relations and inclination of strata that are all linked to the vertical movement, either of the entire basin or its single edges. The configuration of the Main Minibasin with its sag geometry and the stepped onlaps on the basin flanks resembles classic examples of salt withdrawal basins (Jackson & Hudec, 2017). For the interpretation of the basin, we used the concepts presented by Jackson and Hudec (2017) on lateral variations in thickness overburden and their contact relation with the raised structure to decipher the Main Minibasin vertical movement.

Within the Main Minibasin in the study area, Unit A (Figure 6a) exhibits constant thickness and parallel tilted reflectors dipping away from the basement high at the SE. These are clear indicators of an initial

horizontal and plan parallel deposition, that is, the principle of original horizontality, that was then deformed and tilted after the late rising of a deeper layer (i.e. from a posterior uplift of an under/lower deposit), and that is concordant to the non-pierced deeper layer. These indicators show that the deposition was prior to the vertical movement and therefore part of the pre-kinematic stage (Figure 6a). Within Unit B, the same reflector package is seen as a thicker deposit in the depocentre, where subsidence occurs, and a thinner deposit towards the structure growth of the CA (green arrows indicators in Unit B thinning towards SE, Figure 6a). Also, alongside the features D1–D4, reflector terminations for Unit B are discontinuous, cut-off or pinched (e.g. light green arrows NW Figures 6a and 8). This means that accommodation space is created laterally due to the constant rising and the deposits were actively deformed by the uplift. Hence, they were deposited in the syn-kinematic stage. Last, Unit C can be described as the 'draping' deposition, in which the change in thickness is due to the final raised/deformed morphology of the subsurface (Figure 6a). Moreover, no deformation is seen in Unit C reflectors alongside the features D1–D4 (e.g. Figure 6b), suggesting that halokinesis stopped while these sediments were deposited.

The observations on overburden thickness and contact deformation allow us to identify the periods of pre-, syn- and post-kinematic sediment deposition and can be translated into periods of active and inactive vertical movement, and therefore relative timing. Unfortunately, there are no seismic lines that can tie the onlap of the four topographic highs D1 to D4 and provide accurate timing. Also, in spite of their close proximity, it cannot be assumed that sedimentation rates are the same at all four sites since sedimentation is highly influenced by the location of the channels and contourite deposition. However, onlapping reflectors are not present alongside the D3 NE flank (Figure 8). This observation indicates that D3 may still be active or ceased vertical movement only recently pointing to D3 as the last rising diapir. This is consistent with the late timing inferred from the channel C2 deviation (Figure 11c,d).

5.2 | Identification of deformation and evidence for distinct vertical movements

The morphological features of the seafloor such as the structural highs, the changes encountered in the sedimentary processes through channel deviation, canalization, landslides and active tectonics, along with the subsurface structures, such as mass transport deposits, strata cut-off and syn-kinematic deposition; all individually point to active vertical deformation of the seabed in the study area and constrain

relative timing for vertical movement (Section 5.1). In the study area, there are two sets of geological features, that is, the CA and the four isolated basement highs (D1–D4) that indicate uplift and which will be discussed in the following using the term wavelength to describe the lateral extent of the features and the duration of their activity.

5.2.1 | Primary long-wavelength uplift and the Central Area

CA is laterally constricted by two dextral strike-slip faults. The deformation linked to CA covers an area 26 times larger than the isolated basement highs (D1–D4). The seismic stratigraphic configuration of Unit A has NW-dipping concordant plan-parallel reflectors that are unequivocal evidence for prolonged uplift of CA. Moreover, in Unit B, there are at least three dominant and increasingly steeper dips with increasing depth (sub-units b1 to b3; Figure 9). While it is possible that these dips have formed due to progressive deformation and hiatuses, the simplest explanation for the change in dip is that there were at least two phases of uplift. Here, the vertical movement of CA is part of the primary long-wavelength uplift.

Initially, the uplift of CA provided accommodation space for the development of a depocentre NW of it, the Main Minibasin (Figures 6 and 11). This depocentre was filled both by hemipelagic and turbiditic stratified sediments (seen as HARs) and seismically chaotic sediments that we interpret as MTD. These either derive from CA or from further up the Sicily continental slope. Adjacent and on top of Unit A, the buried contouritic features seen in the rim of CA (location of Figure 9 in Figure 2) indicate that CA was uplifted before the sediments were deposited. Throughout the entire time that the basin was infilled, bottom currents interacted with the topographic high of CA and formed sediment waves, moats and drifts indicating an early onset of uplift.

Further evidence for change in topography is provided by the deposition of Fiumefreddo Valley sediments in the deep depocentre west of CA (Main Minibasin) and the late formation of C1 at an almost 90° angle to this sediment input where it straddles the northern rim of CA. We attribute this to a change in sediment transport due to the filling of the accommodation space in the valley and the obstacle posed by CA (Figure 11b).

5.2.2 | Secondary short-wavelength uplift and the features D1–D4

Unlike the CA, the D1-to-D4 features are isolated basement highs with narrow bodies that are elongated or

circular in plan view. They occur adjacent to faults, piercing the seafloor and deforming much smaller areas than CA. That is why we refer to the deformation of D1–D4 as the secondary short-wavelength uplift.

The stratigraphy of the Main Minibasin shows Units A and B are truncated by the isolated basement highs (D1–D4). Especially, the piercing of D2 through Unit A after that unit was tilted by CA demonstrates that D1–D4 formed comparatively fast, late in time and only affected the basin very locally (within 2–4 km areas). The onlapping of Unit C or the lack of it (e.g. adjacent to D3, Figures 7c and 8) shows that deformation was very recent and may still be active.

Small landslide head scarps show indications of recent mass wasting at the flanks of D1, D3 and D4. In between D3 and D4, the backscatter response below the scarps as a bright area points to the lack of hemipelagic deposits, and therefore recent activity. Even though the head scarps are located over the steepest flank of the Central Area, their formation is more likely tied to the late deformation from D3 and D4.

Evidence for late uplift is also provided by the formation of sediment waves at the seafloor adjacent to D4 on its NE flank (Section 5.1). We interpret these sediment waves to be the result of the forced interaction between the LIW bottom current and the seafloor due to the current deviation to the D4 topographic high (Figure 11d). Also, as the Fiumefreddo Valley sedimentation was affected by the CA, an unconfined C2 channel formed initially (Figure 11b). Afterwards, the formation of the topographic high D2 channelized the split flow that resulted in the C2 as we see today on the seafloor and subsurface (Figure 11c). The high-angle bends B5 and B6 of C2 suggest that the channel was later deformed by D3 (Section 5.1). These observations further support that the formation of the isolated highs uplifted the seafloor after the CA (Figure 11d).

5.3 | Uplift origin

Based on all the observations made, along with the recent studies and knowledge of the study area, we explore the geological drivers for the observed uplift. Morphological and stratigraphic evidence for vertical movement point to two different stages (primary and secondary) that have different geological drivers.

5.3.1 | Primary long-wavelength uplift

While the presence of evaporites in the northern part of the Ionian Sea is well-documented (Camerlenghi et al., 2020)

salt diapirism or other forms of halokinesis are unlikely drivers for the observed uplift of CA.

Firstly, the lateral extent of the CA uplifted area is much larger and atypical for salt-related diapirs (>25 km). Secondly, the area surrounding the CA (apart from the main minibasin) does not show the typical seismic reflector configuration of sag basins that are caused by lateral salt withdrawal at depth. Within the Main Minibasin, at the time attributed to the CA uplift, it only shows the progressive tilting of some sedimentary units (Unit A).

On the other hand, considering that the study area is tectonically highly active (Gutscher et al., 2017), strike-slip faults bound the CA and the large wavelength of the main structure, a tectonic origin is likely the mechanism for the primary deformation. The presence of two dextral strike-slip faults north and south of the CA is well established (e.g. Gutscher et al., 2015; Gutscher et al., 2017; Gutscher et al., 2019) and the distance between the strike-slip faults is becoming smaller towards the east. If the southern fault has a larger displacement over time than the northern fault, this would result in wrenching and uplift. Also, the bending of the strike-slip faults may result in push-up, but there is no indication of associated positive flower structures. Without further deep seismic data, the precise tectonic reasons for uplift of this CA remain elusive.

5.3.2 | Secondary short-wavelength uplift (secondary)

Features D1 to D4 have narrow, elongated or circular bodies that occur next to fault systems. They are characterized by chaotic seismic facies at their core, truncation of reflectors on all sides (i.e. piercement) and classical sag basin geometries of the seismic reflectors in the adjacent sedimentary basins, that is, the Main Minibasin (Figure 6a). All this suggests that they are diapirs.

Diapirs are vertically rising geological structures often caused by density inversion. They involve mechanically weak materials, such as shale and salts. Both mud and salt diapirs can be described as an intrusion with discordant contact with the enclosing overburden, vertical bodies and chaotic to transparent facies, which is in great agreement with the characteristics of D1–D4 (Section 4.2). Whether D1–D4 are associated with mud or salt can be further constrained by the seismic data. Mud diapirs are formed by the expulsion of fluids from underlying strata, usually associated with fluid charge, gas and in the instance of mud volcanism by a 'Christmas tree-like' form of extrusion (e.g. Varela & Mohriak, 2013). Here, within the

available seismic data, neither gas nor the distinct 'Christmas tree' shapes are observed in the seismic for the study area. Therefore, a mud diapirism origin seems less likely although it cannot be completely ruled out.

On the other hand, salt diapirs are formed by the rise of ductile salt. The incompressibility, weakness, low density, viscous behaviour and complex shape of salt make it difficult to image (Jones & Davison, 2014). For this reason, salt becomes seismically transparent and the contrast between the sediment and the salt is seen as a high-amplitude contrast. This is similar to what is seen for the features D1–D4, which are seismically transparent bodies, with lateral and top boundaries that show high-amplitude reflections (Section 4.2). The seismic data used in this study also display further attributes that are typical for active salt diapirs. These include (i) upturned collars, (ii) arched roofs and (iii) rims. The first describes upturned or pinched strata near the flanks of salt diapirs, resulting in folding, thickness changes and unconformities (Jackson & Hudec, 2017) as seen along the D1/D2/D3 flanks (e.g. Figures 6a, 7 and 8). The second refers to the strata that have been uplifted and arched above the seafloor (Jackson & Hudec, 2017). Lastly, rims describe a slightly higher seafloor above the roof of adjoining diapirs or pillows (Hudec et al., 2006), as shown in Figure 6a.

The geological background of the area with the Messinian evaporites deposited elsewhere in the study area (Camerlenghi et al., 2020) lends further support to salt diapirism origin. Camerlenghi et al. (2020) predict a salt layer with up to 2 km thickness in the study area. Additionally, the chrono-stratigraphy inferred by us from the comparison with other studies (Section 4.3 and Table 1) places the basement highs within the Miocene with close resemblance to the salt units (Figure 3).

Salt cannot arise spontaneously and movement is only possible upon initiation by local or regional tectonics (e.g. Jackson & Hudec, 2017). Thus, tectonic forces and faults play an important role in the origin of diapirs or vertical structures as they can generate space for the salt to rise (Vendeville & Jackson, 1992). While D1 and D3 are adjacent to the North Alfeo Fault and the nameless fault to the north, D2 and D4 are in between the same two fault systems which in turn also bound the Central Area (Figure 5d).

The imprint of rising salt on the stratigraphy of a basin is controlled by the salt flux and sedimentation rates. Slow aggradation or fast salt flow causes the diapir to rise vertically, having a smaller drape folding zone, that is, a narrow zone of thinning and upturn strata near the diapir (Jackson & Hudec, 2017). These features can be seen along the deformation associated with D1/D2/D3/D4 in the direct vicinity of the basement highs (e.g. Figure 6a). Hence, we interpret the features D1–D4 as the result of halokinesis. Given their elongated shapes in the bathymetric data, diapirs D1, D2 and D3 may be described as salt walls (Jackson & Hudec, 2017; Jackson & Talbot, 1986), while D4 would be commonly referred to as salt stock (Jackson & Hudec, 2017; Jackson & Talbot, 1986).

5.4 | Summary of the timing and interaction of tectonic and sedimentary processes in the study area

From the proxies and processes established above, we can reconstruct the vertical uplift history of the study area as follows. First, tectonic forces caused the slow, long-lasting uplift of CA, referred to here as the primary long-wavelength deformation. The slow rise of CA deformed and tilted the previously horizontal sedimentary Unit A and forced interaction of the seafloor with bottom currents forming moats and drifts (Unit B). This vertical movement caused extension at the crest, which provided space for diapir D4 to rise. The comparatively rapid rise of D4 also led to increases in slope angles and the occurrence of landslides. Additionally, the slow rise of the Central Area deviated the main channel coming from the Fiumefreddo Valley into two channels (C1 and C2). These channels found new paths around CA.

The continuous long-wavelength uplift (i.e. Central Area) provided accommodation space for sediment deposition and formation of the Main Minibasin. The constant sediment input into the Main Minibasin resulted in thick overburden strata.

The increasing sediment depth within the Main Minibasin reached a critical overburden, allowing the underlying evaporates to mobilize causing the sag basin geometry. Due to the density inversion between the filling sediments of the minibasin and the underlying evaporites, salt withdrawal was triggered and formed the diapir feature D2 at the outer rim of CA.

The triggering of halokinesis favoured the rising of salt along the fault systems (zones of weakness that provide the easiest uprising path), forming narrow and vertically isolated topographic highs that rise as a consequence of the tectonic reactivation or density inversion, forming D1 and D3.

6 | CONCLUSION

Analysis of the sedimentary, oceanic and tectonic setting allows constraining the deformation of a morphologically complex part of the upper Calabrian accretionary wedge.

From channel deviations, incision, MTDs, landslide scar, bottom current features and sag basin fill, along with the structural controls, we identify two different vertical movement/uplift patterns. These features serve as proxies for uplift and further provide information on relative timing and a likely genetic origin of the prevailing uplifting processes: a primary long-wavelength uplift of long-term rising over a wide area, and a secondary short-wavelength uplift with short-fast-term uplift and isolated topographic highs. Both stages are intrinsically linked, even though they are driven by different geological processes acting over different time scales. While the primary uplift was due to tectonic forces, the secondary salt uplift was caused by the changes in the sedimentation patterns due to the primary uplift.

Our results support the presence of salt in the NW Ionian Basin as postulated by Camerlenghi et al. (2020) although we cannot fully exclude a mud diapir origin for the diapirs in our study area. Sedimentological and geochemical analyses of pore water samples can help to clarify this in the future. The combined interpretation of seismic and morphological data shows that there are proxies that can be used to decipher vertical motion in complex geological areas. The development of a proxy approach has the potential to help understand sediment deformation and changes caused in ocean basins by vertical movement even in the absence of seismic data. In particular, this will be useful to bridge the gap between short-term seafloor geodetic measurements (Urlaub et al., 2022) and the geological record as it is preserved in seismic data.

CONFLICT OF INTEREST STATEMENT
The authors declare that they have no conflict of interest.

PEER REVIEW
The peer review history for this article is available at https://www.webofscience.com/api/gateway/wos/peer-review/10.1111/bre.12819.

DATA AVAILABILITY STATEMENT
The seismic data are available from the authors upon reasonable request.

ORCID
Bruna T. Pandolpho https://orcid.org/0000-0001-8246-5175
Morelia Urlaub https://orcid.org/0000-0002-1116-636X
Christian Berndt https://orcid.org/0000-0001-5055-0180
Jörg Bialas https://orcid.org/0000-0001-8802-5277

REFERENCES
Argnani, A., & Bonazzi, C. (2005). Malta Escarpment fault zone offshore eastern Sicily: Pliocene-Quaternary tectonic evolution based on new multichannel seismic data. *Tectonics*, *24*, TC4009. https://doi.org/10.1029/2004TC001656

Argnani, A., Mazzarini, F., Bonazzi, C., Bisson, M., & Isola, I. (2013). The deformation offshore of Mount Etna as imaged by multichannel seismic reflection profiles. *Journal of Volcanology and Geothermal Research*, *251*, 50–64. https://doi.org/10.1016/j.jvolgeores.2012.04.016

Barreca, G., Scarfì, L., Gross, F., Monaco, C., & de Guidi, G. (2019). Fault pattern and seismotectonic potential at the south-western edge of the Ionian Subduction system (southern Italy): New field and geophysical constraints. *Tectonophysics*, *761*, 31–45. https://doi.org/10.1016/j.tecto.2019.04.020

Billi, A., Funiciello, R., Minelli, L., Faccenna, C., Neri, G., Orecchio, B., & Presti, D. (2008). On the cause of the 1908 Messina tsunami, southern Italy. *Geophysical Research Letters*, *35*, L06301. https://doi.org/10.1029/2008GL033251

Blumsack, S. L. (1993). A model for the growth of mudwaves in the presence of time-varying currents. *Deep Sea Research Part II: Topical Studies in Oceanography*, *40*, 963–974. https://doi.org/10.1016/0967-0645(93)90043-M

Branca, S., Coltelli, M., & Groppelli, G. (2011). Geological evolution of a complex basaltic stratovolcano: Mount Etna, Italy. *Italian Journal of Geosciences*, *130*, 306–317. https://doi.org/10.3301/IJG.2011.13

Brown, C., Beaudoin, J., Brissette, M., & Gazzola, V. (2019). Multispectral multibeam echo sounder backscatter as a tool for improved seafloor characterization. *Geosciences (Basel)*, *9*, 126. https://doi.org/10.3390/geosciences9030126

Camerlenghi, A., del Ben, A., Hübscher, C., Forlin, E., Geletti, R., Brancatelli, G., Micallef, A., Saule, M., & Facchin, L. (2020).

Seismic markers of the Messinian salinity crisis in the deep Ionian Basin. *Basin Research*, *32*, 716–738. https://doi.org/10.1111/bre.12392

Chapman, R. E. (1983). Chapter 1— Concepts of sedimentary basins. In *Developments in petroleum science* (pp. 1–22). Elsevier. https://doi.org/10.1016/S0376-7361(08)70085-2

Chiocci, F. L., Coltelli, M., Bosman, A., & Cavallaro, D. (2011). Continental margin large-scale instability controlling the flank sliding of Etna volcano. *Earth and Planetary Science Letters*, *305*, 57–64. https://doi.org/10.1016/j.epsl.2011.02.040

Covault, J. A., Sylvester, Z., Hudec, M. R., Ceyhan, C., & Dunlap, D. (2020). Submarine channels 'swept' downstream after bend cutoff in salt basins. *The Depositional Record*, *6*, 259–272. https://doi.org/10.1002/dep2.75

Dellong, D., Klingelhoefer, F., Kopp, H., Graindorge, D., Margheriti, L., Moretti, M., Murphy, S., & Gutscher, M.-A. (2018). Crustal structure of the Ionian Basin and eastern Sicily margin: Results from a wide-angle seismic survey. *Journal of Geophysical Research: Solid Earth*, *123*(3), 2090–2114. https://doi.org/10.1002/2017JB015312

Dillon, C. (2016). *Modelling submerged coastal environments: Remote sensing technologies, techniques, and comparative analysis* (Master). Trent University.

Doughty-Jones, G., Lonergan, L., Mayall, M., & Dee, S. J. (2019). The role of structural growth in controlling the facies and distribution of mass transport deposits in a deep-water salt minibasin. *Marine and Petroleum Geology*, *104*, 106–124. https://doi.org/10.1016/j.marpetgeo.2019.03.015

Faccenna, C., Becker, T. W., Auer, L., Billi, A., Boschi, L., Brun, J. P., Capitanio, F. A., Funiciello, F., Horvàth, F., Jolivet, L., Piromallo, C., Royden, L., Rossetti, F., & Serpelloni, E. (2014). Mantle dynamics in the Mediterranean. *Reviews of Geophysics*, *52*, 283–332. https://doi.org/10.1002/2013RG000444

Flood, R. D. (1988). A lee wave model for deep-sea mudwave activity. *Deep Sea Research Part A. Oceanographic Research Papers*, *35*, 973–983. https://doi.org/10.1016/0198-0149(88)90071-4

Gallais, F., Graindorge, D., Gutscher, M. A., & Klaeschen, D. (2013). Propagation of a lithospheric tear fault (STEP) through the western boundary of the Calabrian accretionary wedge offshore eastern Sicily (Southern Italy). *Tectonophysics*, *602*, 141–152. https://doi.org/10.1016/j.tecto.2012.12.026

Gambino, S. (2022). *Deformation pattern and modelling of active faults along the northern sector of the Malta Escarpment (western Ionian basin)* (PhD). University of Catania. https://doi.org/10.13140/RG.2.2.17355.67363

Gambino, S., Barreca, G., Gross, F., Monaco, C., Gutscher, M., & Alsop, G. I. (2022). Assessing the rate of crustal extension by 2D sequential restoration analysis: A case study from the active portion of the Malta Escarpment. *Basin Research*, *34*(1), 321–341. https://doi.org/10.1111/bre.12621

Gambino, S., Barreca, G., Gross, F., Monaco, C., Krastel, S., & Gutscher, M. A. (2021). Deformation pattern of the northern sector of the Malta escarpment (Offshore SE Sicily, Italy): Fault dimension, slip prediction, and seismotectonic implications. *Front Earth Sci (Lausanne)*, *8*, 1–20. https://doi.org/10.3389/feart.2020.594176

Gross, F., Krastel, S., Geersen, J., Behrmann, J. H., Ridente, D., Chiocci, F. L., Bialas, J., Papenberg, C., Cukur, D., Urlaub, M., & Micallef, A. (2016). The limits of seaward spreading and slope instability at the continental margin offshore Mt Etna, imaged by high-resolution 2D seismic data. *Tectonophysics*, *667*, 63–76. https://doi.org/10.1016/j.tecto.2015.11.011

Gutscher, M.-A., Dellong, D., Dominguez, S., Malavieille, J., Graindorge, D., & Klingelhoefer, F. (2019). Strike-slip faulting in the Calabrian accretionary wedge: Using analog modeling to test the kinematic boundary conditions of geodynamic models. In *Transform plate boundaries and fracture zones* (pp. 321–337). Elsevier. https://doi.org/10.1016/B978-0-12-812064-4.00013-X

Gutscher, M.-A., Dominguez, S., de Lepinay, B. M., Pinheiro, L., Gallais, F., Babonneau, N., Cattaneo, A., le Faou, Y., Barreca, G., Micallef, A., & Rovere, M. (2015). Tectonic expression of an active slab tear from high-resolution seismic and bathymetric data offshore Sicily (Ionian Sea). *Tectonics*, *35*, 39–54. https://doi.org/10.1002/2015TC003898

Gutscher, M.-A., Kopp, H., Krastel, S., Bohrmann, G., Garlan, T., Zaragosi, S., Klaucke, I., Wintersteller, P., Loubrieu, B., le Faou, Y., San Pedro, L., Dominguez, S., Rovere, M., Mercier de Lepinay, B., Ranero, C., & Sallares, V. (2017). Active tectonics of the Calabrian subduction revealed by new multi-beam bathymetric data and high-resolution seismic profiles in the Ionian Sea (Central Mediterranean). *Earth and Planetary Science Letters*, *461*, 61–72. https://doi.org/10.1016/j.epsl.2016.12.020

Hernández-Molina, F. J., de Castro, S., de Weger, W., Duarte, D., Fonnesu, M., Glazkova, T., Kirby, A., Llave, E., Ng, Z. L., Mantilla Muñoz, O., Rodrigues, S., Rodríguez-Tovar, F. J., Thieblemont, A., Viana, A. R., & Yin, S. (2022). Contourites and mixed depositional systems: A paradigm for Deepwater sedimentary environments. In *Deepwater sedimentary systems* (pp. 301–360). Elsevier. https://doi.org/10.1016/B978-0-323-91918-0.00004-9

Hsu, K. J., Montadert, L., Garrison, R. E., Fabricius, F. H., Mueller, C., Cita, M. B., Bizon, G., Wright, R. C., Erickson, A. J., Bernoulli, D., Meliere, F., Kidd, R. B., & Worstell, P. J. (1978). Site 374: Messina Abyssal Plain. In *Initial Reports of the Deep Sea Drilling Project, 42 Pt. 1* (pp. 175–217). U.S. Government Printing Office. https://doi.org/10.2973/dsdp.proc.42-1.105.1978

Hudec, M. R., Jackson, M. P. A., & Schultz-Ela, D. D. (2006). The paradox of minibasin subsidence into salt: Clues to the evolution of crustal basins. *Geological Society of America Bulletin*, *1*, 1. https://doi.org/10.1130/B26275.1

Jackson, M. P. A., & Hudec, M. R. (2017). *Salt tectonics*. Cambridge University Press. https://doi.org/10.1017/9781139003988

Jackson, M. P. A., & Talbot, C. J. (1986). External shapes, strain rates, and dynamics of salt structures. *Geological Society of America Bulletin*, *97*, 305. https://doi.org/10.1130/0016-7606(1986)97<305:ESSRAD>2.0.CO;2

Jones, I. F., & Davison, I. (2014). Seismic imaging in and around salt bodies. *Interpretation*, *2*, SL1–SL20. https://doi.org/10.1190/INT-2014-0033.1

Kokalj, Ž., & Hesse, R. (2017). *Airborne laser scanning raster data visualization, Prostor, kraj, čas*. ZRC SAZU, Založba ZRC. https://doi.org/10.3986/9789612549848

Krastel, S. (2016). RV POSEIDON-CRUISE POS496, Malaga – Catania, 24.03.2016–04.04.2016, Short Cruise Report: MAGOMET—Offshore flank movement of Mount Etna and

associated landslide hazard in the Ionian Sea (Mediterranean Sea). Kiel. https://doi.org/10.3289/SCR_POS_496

Krastel, S., Adami, C., Beier, J., Bialas, J., Bigella, S., Chiocci, F., Crutchley, G., Cukur, D., Frey, B., Fu, L., Gross, F., Gurcay, S., Hempelt, J., Koch, S., Lüttschwager, G., Maisto, F., Masi, L., Matthiesen, T., Micallef, A., … Winkelmann, D. (2012). Seismogenic faults, landslides, and associated tsunamis off southern Italy. Cruise No. M86/2. November 21, 2011 – January 17, 2012 – Cartagena (Spain) – Brindisi (Italy). https://doi.org/10.2312/cr_m86_2

Lurton, X., & Lamarche, G. (2015). Backscatter measurements by seafloor-mapping sonars Guidelines and Recommendations.

Maesano, F. E., Tiberti, M. M., & Basili, R. (2020). Deformation and fault propagation at the lateral termination of a subduction zone: The Alfeo fault system in the Calabrian Arc, Southern Italy. *Frontiers in Earth Science*, *8*, 107. https://doi.org/10.3389/feart.2020.00107

Marani, M., Argnani, A., Roveri, M., & Trincardi, F. (1993). Sediment drifts and erosional surfaces in the central Mediterranean: Seismic evidence of bottom-current activity. *Sedimentary Geology*, *82*, 207–220. https://doi.org/10.1016/0037-0738(93)90122-L

Micallef, A., Camerlenghi, A., Garcia-Castellanos, D., Cunarro Otero, D., Gutscher, M.-A., Barreca, G., Spatola, D., Facchin, L., Geletti, R., Krastel, S., Gross, F., & Urlaub, M. (2018). Evidence of the Zanclean megaflood in the eastern Mediterranean Basin. *Scientific Reports*, *8*, 1078. https://doi.org/10.1038/s41598-018-19446-3

Micallef, A., Krastel, S., & Savini, A. (2018). *Submarine geomorphology, Springer Geology*. Springer International Publishing. https://doi.org/10.1007/978-3-319-57852-1

Micallef, A., Krastel, S., & Savini, A. (2022). Submarine geomorphology. *Geological Society, London, Memoirs*, *58*, 379–394. https://doi.org/10.1144/M58-2021-2

Millot, C., & Taupier-Letage, I. (2005). Circulation in the Mediterranean Sea. In *Life in the Mediterranean Sea: A look at habitat changes* (pp. 29–66). Nova Science Publishers, Inc. https://doi.org/10.1007/b107143

Pepe, F., di Donato, V., Insinga, D., Molisso, F., Faraci, C., Sacchi, M., Dera, R., Ferranti, L., & Passaro, S. (2018). Seismic stratigraphy of upper quaternary shallow-water contourite drifts in the Gulf of Taranto (Ionian Sea, southern Italy). *Marine Geology*, *397*, 79–92. https://doi.org/10.1016/j.margeo.2017.12.004

Polonia, A., Torelli, L., Artoni, A., Carlini, M., Faccenna, C., Ferranti, L., Gasperini, L., Govers, R., Klaeschen, D., Monaco, C., Neri, G., Nijholt, N., Orecchio, B., & Wortel, R. (2016). The Ionian and Alfeo–Etna fault zones: New segments of an evolving plate boundary in the central Mediterranean Sea? *Tectonophysics*, *675*, 69–90. https://doi.org/10.1016/j.tecto.2016.03.016

Polonia, A., Torelli, L., Gasperini, L., Cocchi, L., Muccini, F., Bonatti, E., Hensen, C., Schmidt, M., Romano, S., Artoni, A., & Carlini, M. (2017). Lower plate serpentinite diapirism in the Calabrian Arc subduction complex. *Nature Communications*, *8*, 2172. https://doi.org/10.1038/s41467-017-02273-x

Polonia, A., Torelli, L., Mussoni, P., Gasperini, L., Artoni, A., & Klaeschen, D. (2011). The Calabrian Arc subduction complex in the Ionian Sea: Regional architecture, active deformation, and seismic hazard. *Tectonics*, *30*, TC5018. https://doi.org/10.1029/2010TC002821

Posamentier, H. W., Paumard, V., & Lang, S. C. (2022). Principles of seismic stratigraphy and seismic geomorphology I: Extracting geologic insights from seismic data. *Earth-Science Reviews*. Elsevier B.V., *228*, 103963. https://doi.org/10.1016/j.earscirev.2022.103963

Rebesco, M., Camerlenghi, A., Munari, V., Mosetti, R., Ford, J., Micallef, A., & Facchin, L. (2021). Bottom current-controlled Quaternary sedimentation at the foot of the Malta Escarpment (Ionian Basin, Mediterranean). *Marine Geology*, *441*, 106596. https://doi.org/10.1016/j.margeo.2021.106596

Rebesco, M., Hernández-Molina, F. J., van Rooij, D., & Wåhlin, A. (2014). Contourites and associated sediments controlled by deep-water circulation processes: State-of-the-art and future considerations. *Marine Geology*, *352*, 111–154. https://doi.org/10.1016/j.margeo.2014.03.011

Roveri, M., Flecker, R., Krijgsman, W., Lofi, J., Lugli, S., Manzi, V., Sierro, F. J., Bertini, A., Camerlenghi, A., De Lange, G., Govers, R., Hilgen, F. J., Hübscher, C., Meijer, P. T., & Stoica, M. (2014). The Messinian Salinity Crisis: Past and future of a great challenge for marine sciences. *Marine Geology*, *352*, 25–58. https://doi.org/10.1016/j.margeo.2014.02.002

Ryan, W. B. F., & Heezen, B. C. (1965). Ionian Sea Submarine Canyons and the 1908 Messina turbidity current. *GSA Bulletin*, *76*, 915–932. https://doi.org/10.1130/0016-7606(1965)76[915:ISSCAT]2.0.CO;2

Schambach, L., Grilli, S. T., Tappin, D. R., Gangemi, M. D., & Barbaro, G. (2020). New simulations and understanding of the 1908 Messina tsunami for a dual seismic and deep submarine mass failure source. *Marine Geology*, *421*, 106093. https://doi.org/10.1016/j.margeo.2019.106093

Schattner, U., Lobo, F. J., García, M., Kanari, M., Ramos, R. B., & de Mahiques, M. M. (2018). A detailed look at diapir piercement onto the ocean floor: New evidence from Santos Basin, offshore Brazil. *Marine Geology*, *406*, 98–108. https://doi.org/10.1016/j.margeo.2018.09.014

Skliris, N. (2014). Past, present and future patterns of the thermohaline circulation and characteristic water masses of the Mediterranean Sea. In S. Goffredo & Z. Dubinsky (Eds.), *The Mediterranean Sea* (pp. 29–48). Springer Netherlands. https://doi.org/10.1007/978-94-007-6704-1_3

Solaro, G., Acocella, V., Pepe, S., Ruch, J., Neri, M., & Sansosti, E. (2010). Anatomy of an unstable volcano from InSAR: Multiple processes affecting flank instability at Mt. Etna, 1994–2008. *Journal of Geophysical Research*, *115*, B10405. https://doi.org/10.1029/2009JB000820

Sun, Q., Cartwright, J., Lüdmann, T., Wu, S., & Yao, G. (2017). Three-dimensional seismic characterization of a complex sediment drift in the South China Sea: Evidence for unsteady flow regime. *Sedimentology*, *64*, 832–853. https://doi.org/10.1111/sed.12330

Urlaub, M., Geersen, J., Petersen, F., Gross, F., Bonforte, A., Krastel, S., & Kopp, H. (2022). The submarine boundaries of Mount Etna's unstable southeastern flank. *Frontiers in Earth Science*, *10*, 810790. https://doi.org/10.3389/feart.2022.810790

Varela, C. L., & Mohriak, W. U. (2013). Halokinetic rotating faults, salt intrusions, and seismic pitfalls in the petroleum exploration of divergent margins. *American Association of Petroleum Geologists Bulletin*, *97*, 1421–1446. https://doi.org/10.1306/02261312164

Vendeville, B. C., & Jackson, M. P. A. (1992). The rise of diapirs during thin-skinned extension. *Marine and Petroleum Geology*, *9*, 331–354. https://doi.org/10.1016/0264-8172(92)90047-I

Walbridge, S., Slocum, N., Pobuda, M., & Wright, D. (2018). Unified geomorphological analysis workflows with Benthic Terrain Modeler. *Geosciences (Basel)*, *8*, 94. https://doi.org/10.3390/geosciences8030094

Weiss, A. D. (2001). *Topographic position and landforms analysis*. The Nature Conservancy.

Wynn, R. B., & Stow, D. A. V. (2002). Classification and characterisation of deep-water sediment waves. *Marine Geology*, *192*, 7–22. https://doi.org/10.1016/S0025-3227(02)00547-9

Zakšek, K., Oštir, K., & Kokalj, Ž. (2011). Sky-view factor as a relief visualization technique. *Remote Sensing*, *3*, 398–415. https://doi.org/10.3390/rs3020398